

0

OSCILLATIONS IN TWO-PHASE TWO-COMPONENT FLOW

UNPUBLISHED PRELIMINARY DATA

A. H. STENNING
T. N. VEZIROGLU

FACILITY FORM 902	N67-39310	
	(ACCESSION NUMBER)	(THRU)
	154	0
	(PAGES)	(CODE)
	CR-59504	12
	(NASA CR OR TMX OR AD NUMBER)	(CATEGORY)

October 1964

MECHANICAL ENGINEERING DEPARTMENT
UNIVERSITY OF MIAMI
CORAL GABLES, FLORIDA

NASA GRANT NsG-424
REPORT NO. 4,



OSCILLATIONS IN TWO-PHASE, TWO-COMPONENT FLOW

By A. H. Stenning* and T. N. Veziroglu†

SUMMARY

10065

Experiments with air-water mixtures have been carried out to determine the boundaries of flow oscillations for several ducting configurations. The problem has also been studied analytically with the aid of an analog computer, and a comparison of the experimental and analytical results is presented. Over a wide range of the variables the density ratio for instability is predicted within 30%. The frequency of the oscillations is predicted within 7% for the cases where theoretical values are available.

author

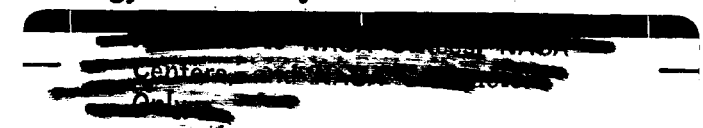
INTRODUCTION

Oscillations in two-phase flows, with and without boiling, have been observed in many systems in which a gas is mixed with a liquid, or a liquid is vaporised [1, 2]. Equipment displaying these oscillations is frequently too complex to permit comparison of the observed behavior with theory, and in consequence a great deal of experimental information has been gathered which cannot be correlated.

The objective of this investigation was to study two-phase flow oscillations in an extremely simple flow configuration. A two-component two-phase flow system offers some experimental advantages over a one-

* Professor of Mechanical Engineering, University of Miami, Coral Gables, Florida.

† Associate Professor of Mechanical Engineering, University of Miami.



component two-phase flow system with boiling since the flow rate of each phase can be independently controlled and measured, and the uncertainties of boiling heat transfer are avoided. Air and water were selected as the components.

ANALYSIS

The geometry of the model used for the theoretical investigation was similar to the experimental test section, and is shown in Figure 1(a). Liquid (water in this case) flows through an entrance duct and a valve to a mixer which simulates a boiler. In the mixer a gas (air) is bubbled into the liquid through a porous tube at a constant rate. The mixture flows through an exit duct and out of an orifice. The total pressure drop across the system is constant and gravitational effects are neglected.

For analysis, the system was broken up into four segments; one for the inlet ducting including the inlet valve, two equal segments for the mixer section and one for the exit ducting. The number of segments was limited to four by the non-linear components available in the analog computer used, an EAI TR-48, but previous studies of lumping accuracy showed this number to be satisfactory for the density ratios used.

The assumptions and method of analysis were similar to that employed in [3]. Lumped continuity equations were written for each segment, and the overall pressure drop was represented as the sum of the component pressure drops and the pressure drop required to accelerate the flow during oscillations. Homogeneous flow was assumed, and the gas density in the mixer and duct was assumed to be constant during the oscillations.

Continuity

For the n^{th} lump, as shown in Figure 1(b), the continuity equation may be approximated as,

$$\rho_n U_n A_n - \rho_{n+1} U_{n+1} A_{n+1} = \frac{V_n}{2} \cdot \frac{d}{dt} (\rho_n + \rho_{n+1}) \quad (1)$$

where ρ is density, U flow velocity, A flow area, V the segment volume and t is time. The mass of the injected gas is neglected, since it was less than 1% of the liquid mass flow rate in the experiments.

Dividing both sides of equation (1) by $\rho_1 U_{1s} A_1$ where ρ_1 is the liquid density, A_1 the cross-sectional area and U_{1s} the steady state velocity at the entrance to the mixer, we obtain,

$$r_n u_n - r_{n+1} u_{n+1} = \frac{V_n}{2 U_{1s} A_1} \cdot \frac{d}{dt} (r_n + r_{n+1}) \quad (2)$$

where $r = \frac{\rho}{\rho_1}$

and $u = \frac{UA}{U_{1s} A_1} \left(= \frac{U}{U_{1s}} \text{ for uniform cross-sectional area} \right)$

Normalizing V_n with respect to the mixer volume V_m and introducing a normalized time T , equation (2) becomes,

$$r_n u_n - r_{n+1} u_{n+1} = v_n \cdot \frac{d}{dT} (r_n + r_{n+1}) \quad (3)$$

where $v = \frac{V}{V_m} \left(= \frac{L}{L_m} \text{ for uniform cross-sectional area} \right)$

and $T = \frac{2 U_{1s} A_1}{V_m} \cdot t \left(= \frac{2 U_{1s}}{L_m} \cdot t \text{ for uniform cross-sectional area} \right)$

At steady state,

$$r_{(n+1)s} u_{(n+1)s} = r_{ns} u_{ns} = r_1 u_{1s} = 1$$

since $r_1 = 1$ and $u_{1s} = 1$.

Assuming that the gas is introduced into the liquid at a constant rate and uniformly along the mixer, the following volume flow rate relationship is obtained for the segments 1 and 2:

$$U_{n+1} A_{n+1} - U_n A_n = Q_n \quad (4)$$

where Q_n is the volume rate of gas injection into the n^{th} segment.

Dividing both sides of equation (4) by $U_{1s} A_1$,

$$u_{n+1} - u_n = q_n \quad (5)$$

where $q = \frac{Q}{U_{1s} A_1}$, the normalized volume rate of gas introduction.

In our particular case, since the two mixer segments are of equal size, let

$$q_1 = q_2 = q_0 \quad (6)$$

From equations (5) and (6), the equations applicable to the individual mixer segments are given by,

$$u_2 - u_1 = q_0 \quad (7)$$

$$\text{and} \quad u_3 - u_2 = q_0 \quad (8)$$

The corresponding equation for the segments 0 and 4, would

$$\text{yield} \quad u_1 - u_0 = 0 \quad (9)$$

$$\text{and} \quad u_4 - u_3 = 0 \quad (10)$$

since no gas is introduced into those segments and gas compressibility is neglected.

Eliminating u_2 and u_3 between equations (7), (8) and (10),

$$u_4 - u_1 = 2q_0 \quad (11)$$

At steady state,

$$u_{1s} = 1$$

$$\text{and} \quad u_{4s} = \frac{1}{r_{4s}}$$

where r_{4s} is the overall density ratio. Hence equation (11) yields the following relationship between q_0 and r_{4s} :

$$q_0 = \frac{1}{2r_{4s}} - \frac{1}{2} \quad (12)$$

$$\text{or} \quad r_{4s} = \frac{1}{1 + 2q_0} \quad (13)$$

Pressure Drop

In calculating the total pressure drop, the system was divided into three sections - the first consisting of the entrance ducting and inlet valve where there is no density change (segment 0), the second consisting of the mixer and the exit ducting where large density and velocity changes take place (segments 1 through 3), and the third being the exit orifice.

For an incompressible liquid, the pressure drop ($P_0 - P_1$) across the segment O is the sum of the frictional pressure drop in the ducting, the pressure drop across the inlet valve and the inertial pressure drop, i.e.,

$$P_0 - P_1 = K_0' \rho_1 U_1^2 + K_0'' \rho_1 U_1^2 + L_1 \rho_1 \frac{dU_1}{dt} \quad (14)$$

where the coefficient K_0' is a function of the inlet ducting configuration and roughness, the coefficient K_0'' a function of the valve opening, and the length L_1 the equivalent length for the inlet ducting. The equivalent length L_1 is given by,

$$L_1 = A_1 \sum \frac{L}{A}$$

where $\sum \frac{L}{A}$ is summed for all the entrance ducting.

Similarly, for a constant cross-sectional area mixer and exit ducting the pressure drop is,

$$P_1 - P_4 = \text{Frictional Pressure Drop} + \text{Momentum Pressure Drop} \\ + \text{Inertial Pressure Drop}$$

$$\text{or } P_1 - P_4 = K_{me} \left(\frac{\rho_1 U_1^2 + \rho_4 U_4^2}{2} \right) + (\rho_4 U_4^2 - \rho_1 U_1^2) \\ + L_{me} \frac{d}{dt} \left(\frac{\rho_1 U_1 + \rho_4 U_4}{2} \right) \quad (15)$$

$$\text{where } K_{me} = \frac{l f_{me} L_{me}}{D_{me}}$$

L_{me} = Mixer length plus exit ducting length,

f_{me} = Effective coefficient of friction for the mixer and exit ducting,

and D_{me} = Hydraulic diameter for the mixer and exit ducting.

The pressure drop across the exit orifice is expressed by the equation,

$$P_4 - P_5 = K_4 \rho_4 U_4^2 \quad (16)$$

assuming that a relationship of this type is still useful for two-phase flow.

Let us now normalize the pressure drop equations with respect to the steady state pressure at station 1, P_{1s} . Dividing equation (14) by P_{1s} , and normalizing U_1 ,

$$p_o - p_1 = \frac{(K_o' + K_o'') \rho_1 U_{1s}^2 u_1^2}{P_{1s}} + \frac{L_1 \rho_1 U_{1s}}{P_{1s}} \cdot \frac{du_1}{dt} \quad (17)$$

where $p = \frac{P}{P_{1s}}$

and $u_1 = \frac{U_1 A_1}{U_{1s} A_1} = \frac{U_1}{U_{1s}}$

Introducing the normalized time T and normalizing L_1 with respect to the mixer length L_m , equation (17) reduces to,

$$p_o - p_1 = \frac{(K_o' + K_o'') \rho_1 U_{1s}^2 u_1^2}{P_{1s}} + 2 l_1 p'_d \frac{du_1}{dT} \quad (18)$$

where the normalized length of inlet ducting is given by,

$$l_1 = \frac{L_1}{L_m}$$

and the dynamic pressure normalized with respect to P_{1s} , is defined as,

$$p'_d = \frac{\rho_1 U_{1s}^2}{P_{1s}}$$

At steady state, equation (18) yields,

$$\frac{(K_o' + K_o'') \rho_1 U_{1s}^2}{P_{1s}} = p_o - 1 \quad (19)$$

Substituting equation (19) in (18),

$$p_o - p_1 = (p_o - 1) u_1^2 + 2 \ell_1 p'_d \frac{du_1}{dT} \quad (20)$$

Dividing equation (15) by P_{1s} , and rearranging,

$$\begin{aligned} p_1 - p_4 &= \frac{(K_{me} - 2) \rho_1 U_{1s}^2}{2 P_{1s}} u_1^2 + \frac{(K_{me} + 2) \rho_1 U_{1s}^2}{2 P_{1s}} r_4 u_4^2 \\ &+ (1 + \ell_e) p'_d \frac{d}{dT} (u_1 + r_4 u_4) \end{aligned} \quad (21)$$

where the normalized exit ducting length is defined as,

$$\ell_e = \frac{\text{Exit ducting length, } L_e}{\text{Mixer Length, } L_m}$$

At steady state, equation (21) yields,

$$K_{me} = \frac{2(1 - p_{4s}) r_{4s} + 2(r_{4s} - 1) p'_d}{(1 + r_{4s}) p'_d} \quad (22)$$

Substituting equation (22) in (21),

$$p_1 - p_4 = \frac{(1 - p_{4s}) r_{4s} - 2 p'_d}{1 + r_{4s}} u_1^2 + \frac{(1 - p_{4s}) r_{4s} + 2 r_{4s} p'_d}{1 + r_{4s}} r_4 u_4^2 + (1 + \ell_e) p'_d \frac{d}{dT} (u_1 + r_4 u_4) \quad (23)$$

Similarly the normalized form of equation (16) becomes,

$$p_4 - p_5 = (p_{4s} - p_5) r_{4s} r_4 u_4^2 \quad (24)$$

Summing up equations (20), (23), and (24) and thereby eliminating the variables p_1 and p_4 , the total normalized pressure drop across the system becomes,

$$p_o - p_5 = \left[p_o - \frac{1 + r_{4s} p_{4s} + 2 p'_d}{1 + r_{4s}} \right] u_1^2 + \left[\frac{(1 - p_{4s}) r_{4s} + 2 r_{4s} p'_d}{1 + r_{4s}} + (p_{4s} - p_5) r_{4s} \right] r_4 u_4^2 + p'_d \frac{d}{dT} \left[(1 + \ell_e + 2 \ell_i) u_1 + (1 + \ell_e) r_4 u_4 \right] \quad (25)$$

Noting that $p'_d \ll 1$, $r_{4s} < 1$ and assuming a relatively large pressure drop across the exit orifice compared to that of the mixer and exit ducting (i.e., $p_{4s} \approx 1$), equation (25) reduces to,

$$p_o - p_5 = (p_o - 1) u_1^2 + (1 - p_5) r_{4s} r_4 u_4^2 + p'_d \frac{d}{dT} \left[(1 + \ell_e + 2 \ell_i) u_1 + (1 + \ell_e) r_4 u_4 \right] \quad (26)$$

Dividing both sides of equation (26) by the normalized constant pressure drop across the system, $p_o - p_5$,

$$1 = y u_1^2 + (1 - y) r_{hs} r_h u_h^2 + p_d \frac{d}{dT} \left[(1 + l_e + 2l_i) u_1 + (1 + l_e) r_h u_h \right] \quad (27)$$

where $y = \frac{p_o - p_{1s}}{p_o - p_5}$, the pressure drop fraction attributable to the upstream side, and $p_d = \frac{\rho_1 u_{1s}^2}{p_o - p_5}$, the dynamic pressure normalized with respect to the overall pressure drop.

The analog computer block diagram for scaled versions of the equations (3), (7), (8), (9), (10), (13), and (27) is shown in Figure 2. The conventional symbols are used for components with A denoting a summer, I an integrator, M a multiplier, D a divider, X^2 a squarer, P a coefficient potentiometer, In an inverter and S a constant voltage source. In accordance with the block diagram, the above equations were then programmed for an EAI TR - 48 Analog Computer. The equations were not linearised.

General Stability Study

As seen from the equations (3), (7), (8), (9), (10), (13), and (27), there are five variables governing stability, namely the normalized inlet ducting length $l_i = L_i/L_m$, the normalized exit ducting length $l_e = L_e/L_m$, the steady state overall density ratio $r_{hs} = \rho_{hs}/\rho_1$, inlet pressure drop fraction $y = \frac{p_o - p_{1s}}{p_o - p_5}$, and the normalized steady state dynamic pressure $p_d = \frac{\rho_1 u_{1s}^2}{p_o - p_5}$. The computer block diagram (Fig. 2) shows that it is

convenient to fix the values of l_1 , l_e , p_d and y , and to vary the overall density ratio r_{hs} to obtain the onset of instability since r_{hs} can be controlled by means of one potentiometer only with no other adjustments needed. Consequently, during each series of computer runs the parameter r_{hs} was varied to obtain its value at the stability boundary while the remaining variables were kept constant. The onset of instability was determined by observing an oscilloscope image of density (or velocity) voltage at one of the stations, usually the station at the end of the mixer, and adjusting the density ratio r_{hs} till small oscillations were barely visible. No hysteresis effect was noted, that is the stability boundary was the same when approached from the stable or unstable sides. Altogether 57 series of computer runs were carried out. The values of l_1 used were between 0.5 and 8, l_e between 0.2 and 5, $1/r_{hs}$ between 3 and 13, y between 0 and 0.26, and p_d between 0 and 0.03. These values were selected to cover the range of parameters encountered in the air-water experiments. The results are plotted in Figures 3 through 11. The region above each curve is unstable, and below each curve is stable.

DISCUSSION

Figure 3 shows the relationship between the overall density ratio $\rho_1/\rho_{hs}(1/r_{hs})$ and the normalized inlet ducting length l_1 at the stability boundary for different values of the inlet pressure drop fraction y with p_d constant and equal to 0.015, and l_e constant and equal to 1.5. With the exception of a small counter-trend for low values of l_1 at $y = 0.13$, increasing the length of the inlet ducting increases the range

of density ratios for which the system is stable. Since the fluid inertia (and hence the resistance to flow changes) of the system increases with l_1 , this trend is not surprising.

In Figure 4, the effect of exit ducting length l_e on stability is shown for $p_d = 0.015$, $l_1 = 4.5$. The range of stable density ratios decreases as the exit duct length is increased, approaching a different asymptotic value for very long ducts at each value of y . This destabilizing effect is caused by the transport time delay in density changes between the end of the mixer and the orifice.

Figures 5 through 11 show the stability maps - the relationship between ρ_1/ρ_{lg} and p_d at the stability boundary - for various combinations of l_1 , l_e and y . The parameter p_d enters the equations as a factor in the effective fluid inertia, and hence an increase in p_d helps to stabilize the system. The small destabilizing trend sometimes found at low values of p_d is unexpected and may be a consequence of small cumulative errors in the computer. Increasing the inlet side pressure drop always helps to stabilize the system, due to the damping effect on flow changes.

EXPERIMENTAL PROGRAM

The air-water two-phase flow test section is shown in Figure 12. It consisted of a surge tank, inlet ducting, inlet valve, mixer, outlet ducting and the exit orifice. Water entered the test-section from the surge tank at pressures up to 40 psig and flowed through the inlet ducting and inlet valve into the inner tube of the mixer. The pressurized air supplied to the jacket of the mixer seeped through the porous bronze inner tube and bubbled into the water. The two-phase mixture then flowed through the outlet ducting and out of the rounded exit orifice.

The pressure drop across the walls of the porous bronze tube was so large (about 40 psi) that the air flow rate was insensitive to oscillations in test section pressure.

The surge tank damped out any fluctuations in the water supply and provided a constant pressure drop across the test section, while the inlet valve was used to control the inlet pressure drop. The exit duct was made of clear lucite tube for observation of the two-phase flow and the oscillations. It was prepared in several lengths up to 22 inches with an inner diameter of $5/8$ inch, the same as that of the porous bronze tube in the mixer. To study the effect of orifice size, three exit orifice pieces were constructed with $1/8$ inch, $3/16$ inch and $1/4$ inch diameter nozzles.

Figure 13 is a sketch showing the complete experimental set up and the instrumentation. Air was supplied through the high pressure compressed air system in the laboratory, which provided air at constant pressure, and water was circulated by a motor driven centrifugal pump. Air and water flow rates were controlled by a needle valve and a wedge-gate valve respectively. The water flow rate was measured by a Potter turbine type flow meter and the air flow rate by a Vol-O-Flow flowmeter. Bourdon type Heise pressure gages were used to measure the pressures along the inlet ducting, in the air jacket and at other stations as indicated in the sketch. To observe and record the two-phase flow oscillations, two Giannini pressure transducers were placed at the upstream and downstream sides of the lucite outlet tubing. These pressures were recorded on two chart recorders, and fluctuations in water flow rate were also recorded on a chart recorder. The maximum error in measured density ratio was estimated as $\pm 4\%$.

Experimental Procedure

In experiments to determine the onset of oscillations and the influence of the parameters affecting the oscillations air was first run through the system at a low flow rate, and then the water pump was started. This prevented water from entering the air jacket.

After this, the air flow was increased in small steps till the onset of two-phase flow oscillations was observed. These oscillations could be observed visually through the lucite outlet tubing and also on the pressure recorders. At the stability boundary, reached from the stable region as described above, room temperature, barometric pressure, air and water flow rates and the pressures at various stations were recorded. Then the air flow rate was further increased to operate in the unstable region and to obtain chart recordings of the pressures for frequency calculations. In addition, the temperature, mean flow and mean pressure readings were taken. After this, by reducing the air flow the stability boundary was reached from the unstable region. A new set of readings was also taken at this stage. Experiments were repeated by varying the inlet pressure drops for each length of outlet ducting and each orifice size.

A well-mixed bubbly flow was observed in the test section at steady state operation. When the stability boundary was crossed, the water flow rate immediately began to oscillate with an amplitude roughly 40% of the mean flow rate (Fig. 14) and alternating bubbly slugs containing mostly air or mostly water were observed in the lucite duct. Reducing the mean water flow rate or increasing the air flow rate to move further into the unstable regime produced some increase in the amplitude of the

water flow oscillations, but little change in frequency. The air flow rate was unaffected by the oscillations, and the pressure in the test section oscillated with a maximum amplitude of approximately 1 psi. The frequency was of the order of 1 cps. Except for the 1/4" orifice, the pressure drop in the mixer and duct was less than 5% of the overall pressure drop.

To check the validity of the assumption made in the analysis that the usual orifice equation (Equation (16)) applicable to single-phase fluid flow is also good for two-phase flow with the orifice sizes used in the experiments, a set of steady flow experiments was carried out. In these experiments, air and water mixtures were run through each orifice at steady state and the air and water flow rates and the orifice pressure drop were recorded.

Experimental Results

The results of the experiments to determine the circumstances under which equation (16) is valid, are plotted in Figures 15 through 17 for each orifice size as the mean two-phase velocity at station 4, U_{4s} , versus orifice pressure drop divided by mixture density at exit, $\frac{\Delta p_{or}}{\rho_{4s}}$.

The orifice equations obtained from the best line through the experimental points are given in the Figures. For the conventional orifice equation (16), U_{4s} is proportional to $\left(\frac{\Delta p_{or}}{\rho_{4s}}\right)^{0.5}$.

As seen from the Figures, the 1/8" diameter orifice had a flow characteristic close to the assumed relation, with an exponent of 0.485 instead of 0.5. The 3/16" diameter orifice also gave fair agreement with the assumed relation, with an exponent of 0.474. The departure from the

assumed relation was largest in the case of the $1/4$ " diameter orifice. Consequently, it would be expected that the best agreement between theory and experiments would be obtained with the two smaller orifices.

The results of the stability boundary experiments are plotted in Figures 18 through 28 as the overall density ratio (liquid density divided by the mixture density at exit) versus the inlet pressure drop fraction (inlet pressure drop divided by the total pressure drop) at the onset of the oscillations and also during the oscillations for various outlet duct lengths and orifice sizes.

There is no distinguishable hysteresis effect. Although there is some scattering of points at the boundary, it seems that the same mean boundary is obtained whether approached from the stable or unstable regions. All the points corresponding to unstable operation have a higher overall density ratio for a given y than the points at the stability boundary.

Measurements of the oscillation frequency were made near the stability boundary, and the results of these measurements are plotted in Figure 29 in dimensionless form as $\frac{\delta U_{4s}}{L_{me}}$ versus l_e for different values of y , where δ is the time period of the oscillation, L_{me} the total length of mixer plus exit duct, U_{4s} the mean velocity at the end of the exit duct.

Comparison of Experiments with Theory

On Figures 18 through 28, the stability boundary curves obtained from the analysis are superimposed. The coordinates $(1/r_{4s}, y)$ of the points of the theoretical curve were obtained from the theoretical stability maps (Figs. 6 through 12) corresponding to the parameters

(l_1, l_e, p_d) of the experimental points. The points so determined were then plotted on the corresponding Figures of the experimental results to obtain the theoretical curves. The value of l_1 for the apparatus was 3.46.

The best experimental curve for the stability boundary is also drawn in each Figure. These curves were obtained by joining the experimental points nearer to the stable region (i.e., the points corresponding to lower overall density ratios for a given inlet pressure drop fraction) instead of drawing them through the mean of all the boundary points. This was done because, as explained above, the stability boundary depends on the detection of small oscillations by the observer. It is therefore expected that due to human error some of these "boundary" points may really be in the unstable region and the true stability boundary is probably the lower envelope of all the onset measurements. It should be noted that since no computer data was available for $l_e = 0$, the corresponding $(1/r_{Lg}$ versus y) analytical curve could not be plotted in Figure 28.

In comparing the stability theory and the experimental results, the following observations can be made:

1. For small values of inlet pressure drop fraction y ($y < 0.08$) the agreement between the theory and the experiments is good. The divergence is less than $\pm 10\%$.
2. For values of inlet pressure drop fraction y between 0.08 and 0.16 the divergence is greater - up to 30%, the theoretical prediction of stability boundary being conservative; i.e., the actual systems are more stable than indicated by the theory. This could be caused by slip between the gas and liquid, which is neglected in the analysis,

but there is no reason to expect slip effects to be more important in this region than at small values of y . The departure of the actual orifice characteristics from the theoretical equation tends to stabilize the system.

3. The theoretical and experimental stability curves meet at a value of inlet pressure drop fraction y around 0.16, and further closure of the inlet valve does not change the density ratio at which instability occurs. This behavior is at variance with the theoretical curves, which continue to show some increase in stability with increasing y . It is possible that cavitation occurred in the inlet valve for the higher values of inlet pressure drop, producing a vapor cavity which decoupled the valve flow from the flow oscillations in the test section. A similar phenomenon was observed in a Freon boiling rig when cavitation occurred between the inlet valve and the boiler. With the $1/4$ " orifice, the minimum value of y attainable was 0.10, due to the relatively large effect of inlet piping losses with this configuration. In consequence, it was not possible to compare theory and experiment in the region of y where agreement was good for the $1/8$ " and $1/4$ " orifices. The stability boundary was completely insensitive to y for the $1/4$ " orifice, and since the water flow rate was greatest and the water pressure lowest (about 10 psig) for this configuration, inlet valve cavitation was most likely to occur with the $1/4$ " orifice.

Analog computer measurements of predicted oscillation frequency were made only for the case of zero inlet pressure drop, and these predictions are shown on Figure 29. Agreement with the experimental data is excellent,

with a maximum error of 7% in the predicted frequency. Increasing the inlet pressure drop has the effect of increasing the dimensionless time period of the oscillations, due to the longer particle residence time which accompanies the increased density ratio at the stability boundary.

CONCLUSIONS

The assumed model of transient flow behavior reproduces the major features of two-phase flow instability in a simple air-water system. Further work on the detailed flow pattern in the test section is necessary to improve the accuracy of the theoretical stability boundary.

ACKNOWLEDGEMENTS

The authors wish to acknowledge the contributions made by Mr. G. Callahan and Mr. T. C. Wang, graduate students at the University of Miami, who carried out the experiments with the air-water apparatus.

The research was sponsored by the National Aeronautics and Space Administration, under Grant No. NSG-424.

APPENDIX - SYMBOLS

A	flow area
D	hydraulic diameter or diameter
f	coefficient of friction
K	pressure drop constant
l	normalized length
L	length
p	normalized pressure
P	pressure
q	normalized volume rate of gas injection
Q	volume rate of gas injection
r	density divided by liquid density
t	time
T	normalized time
u	normalized volume flow rate or normalized velocity
U	velocity
v	normalized volume
V	volume
y	normalized upstream pressure drop
δ	period of oscillations
ρ	density

Subscripts:

d	dynamic
e	exit ducting
i	inlet ducting
m	mixer
me	mixer plus exit ducting
n	number of lump or station
or	orifice
s	steady state

REFERENCES

1. Wallis, G. B., and Heasley, J. H.: "Oscillations in Two-Phase Flow Systems". Journal of Heat Transfer, Trans. ASME, Series C, vol. 83, August 1961 pp. 363-369.
2. Stenning, A. H.: "Instabilities in the Flow of a Boiling Liquid". Journal of Basic Engineering, Trans. ASME, Series D, vol. 86, June 1964, pp. 213-217.
3. Stenning, A. H., and Veziroglu, T. N.: "A Parametric Study of Boiling Instability". To be presented at the ASME Annual Meeting, Nov. 1964.

LIST OF FIGURES

- Figure 1(a).- System under Consideration
- Figure 1(b).- Portion of System
- Figure 2.- Analog Computer Block Diagram
- Figure 3.- Overall Density Ratio vs. Normalized Inlet Ducting Length at Stability Boundary ($l_e = 1.5$, $p_d = 0.015$)
- Figure 4.- Overall Density Ratio vs. Normalized Exit Ducting Length at Stability Boundary ($l_e = 4.5$, $p_d = 0.015$)
- Figure 5.- Overall Density Ratio vs. Normalized Dynamic Pressure at Stability Boundary ($l_1 = 2.5$, $l_e = 0.2$)
- Figure 6.- Overall Density Ratio vs. Normalized Dynamic Pressure at Stability Boundary ($l_1 = 2.5$, $l_e = 0.5$)
- Figure 7.- Overall Density Ratio vs. Normalized Dynamic Pressure at Stability Boundary ($l_1 = 2.5$, $l_e = 1.0$)
- Figure 8.- Overall Density Ratio vs. Normalized Dynamic Pressure at Stability Boundary ($l_1 = 2.5$, $l_e = 1.5$)
- Figure 9.- Overall Density Ratio vs. Normalized Dynamic Pressure at Stability Boundary ($l_1 = 3.17$, $l_e = 2.17$)
- Figure 10.- Overall Density Ratio vs. Normalized Dynamic Pressure at Stability Boundary ($l_1 = 3.67$, $l_e = 2.67$)
- Figure 11.- Overall Density Ratio vs. Normalized Dynamic Pressure at Stability Boundary ($l_1 = 4.5$, $l_e = 3.5$)
- Figure 12.- Air-Water Apparatus Test Section
- Figure 13.- Schematic Diagram of Experimental Set-Up for Two-Phase Instability (Air-Water Apparatus)

- Figure 14.- A Recording of Water Mass Flow Rate Oscillations
Near Stability Boundary
- Figure 15.- 1/8" Diameter Orifice Calibration for Two-Phase Flow
- Figure 16.- 3/16" Diameter Orifice Calibration for Two-Phase Flow
- Figure 17.- 1/4" Diameter Orifice Calibration for Two-Phase Flow
- Figure 18.- Experimental and Theoretical Stability Boundary
($L_e = 22$ in., $D_{or} = 1/8$ in.)
- Figure 19.- Experimental and Theoretical Stability Boundary
($L_e = 22$ in., $D_{or} = 3/16$ in.)
- Figure 20.- Experimental and Theoretical Stability Boundary
($L_e = 22$ in., $D_{or} = 1/4$ in.)
- Figure 21.- Experimental and Theoretical Stability Boundary
($L_e = 15$ in., $D_{or} = 1/8$ in.)
- Figure 22.- Experimental and Theoretical Stability Boundary
($L_e = 15$ in., $D_{or} = 3/16$ in.)
- Figure 23.- Experimental and Theoretical Stability Boundary
($L_e = 15$ in., $D_{or} = 1/4$ in.)
- Figure 24.- Experimental and Theoretical Stability Boundary
($L_e = 9$ in., $D_{or} = 1/8$ in.)
- Figure 25.- Experimental and Theoretical Stability Boundary
($L_e = 9$ in., $D_{or} = 3/16$ in.)
- Figure 26.- Experimental and Theoretical Stability Boundary
($L_e = 4$ in., $D_{or} = 1/8$ in.)
- Figure 27.- Experimental and Theoretical Stability Boundary
($L_e = 4$ in., $D_{or} = 3/16$ in.)

Figure 28.- Experimental and Theoretical Stability Boundary

($L_e = 0$, $D_{or} = 1/8$ in.)

Figure 29.- Time Period of Oscillations at Stability Boundary

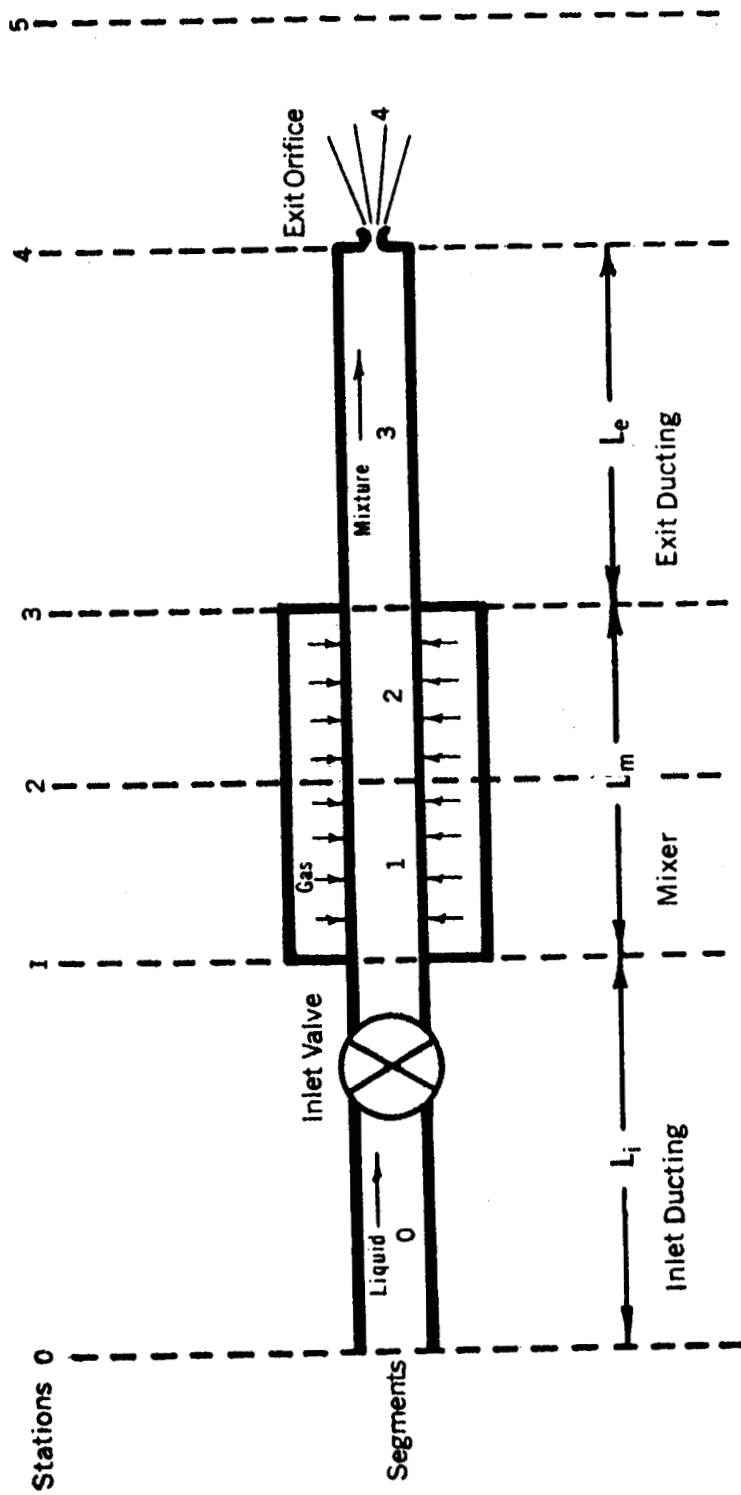


FIG. 1(A).—SYSTEM UNDER CONSIDERATION

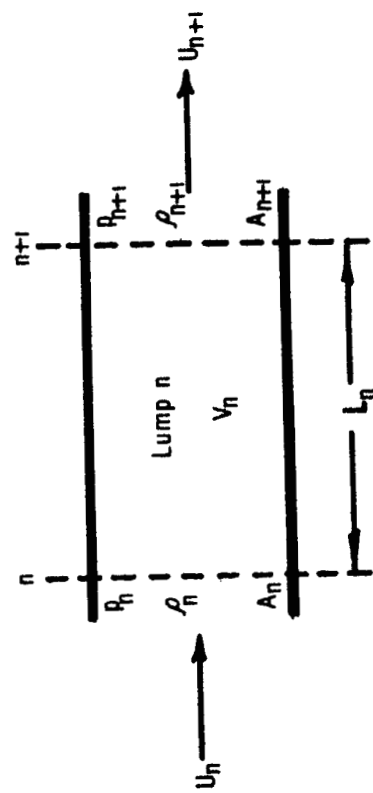


FIG. 1(B).—PORTION OF SYSTEM

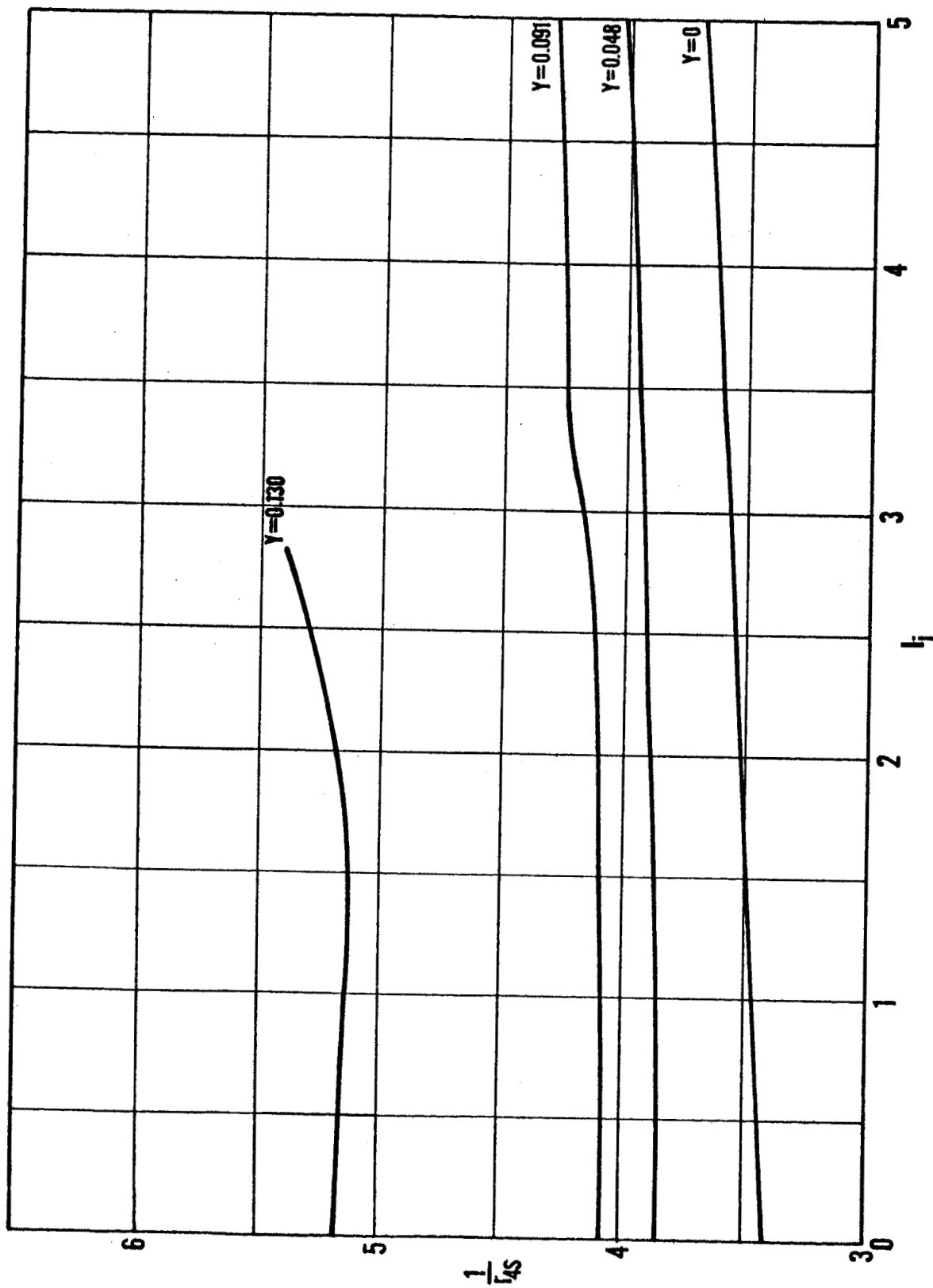


FIG. 3.— OVERALL DENSITY RATIO VS NORMALIZED INLET DUCTING LENGTH AT STABILITY BOUNDARY
 ($l_e=1.5$, $p_d=0.015$)

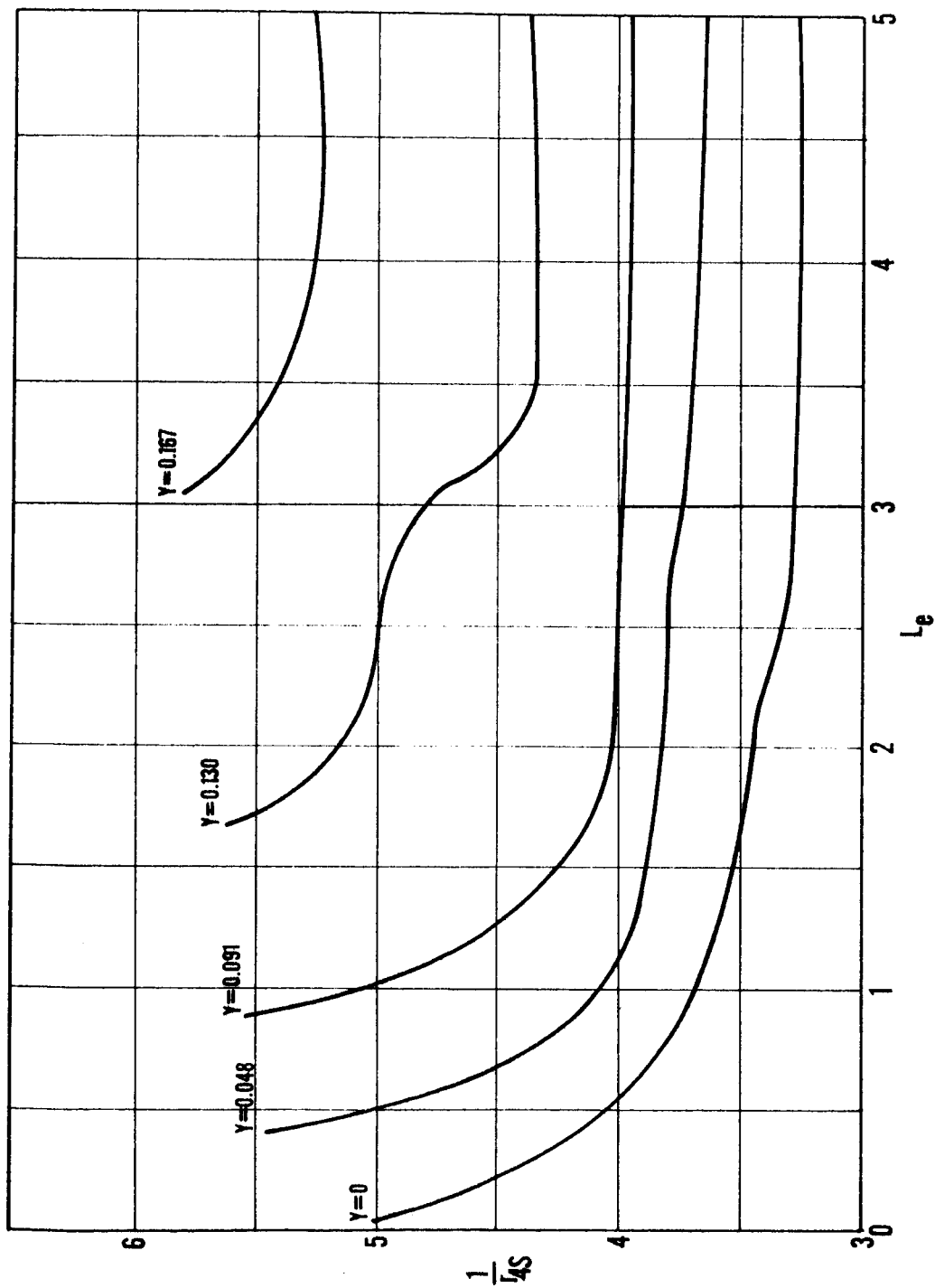


FIG. 4.- OVERALL DENSITY RATIO VS NORMALIZED EXIT DUCTING LENGTH AT STABILITY BOUNDARY
 ($i_1=4.5$, $P_d=0.015$)

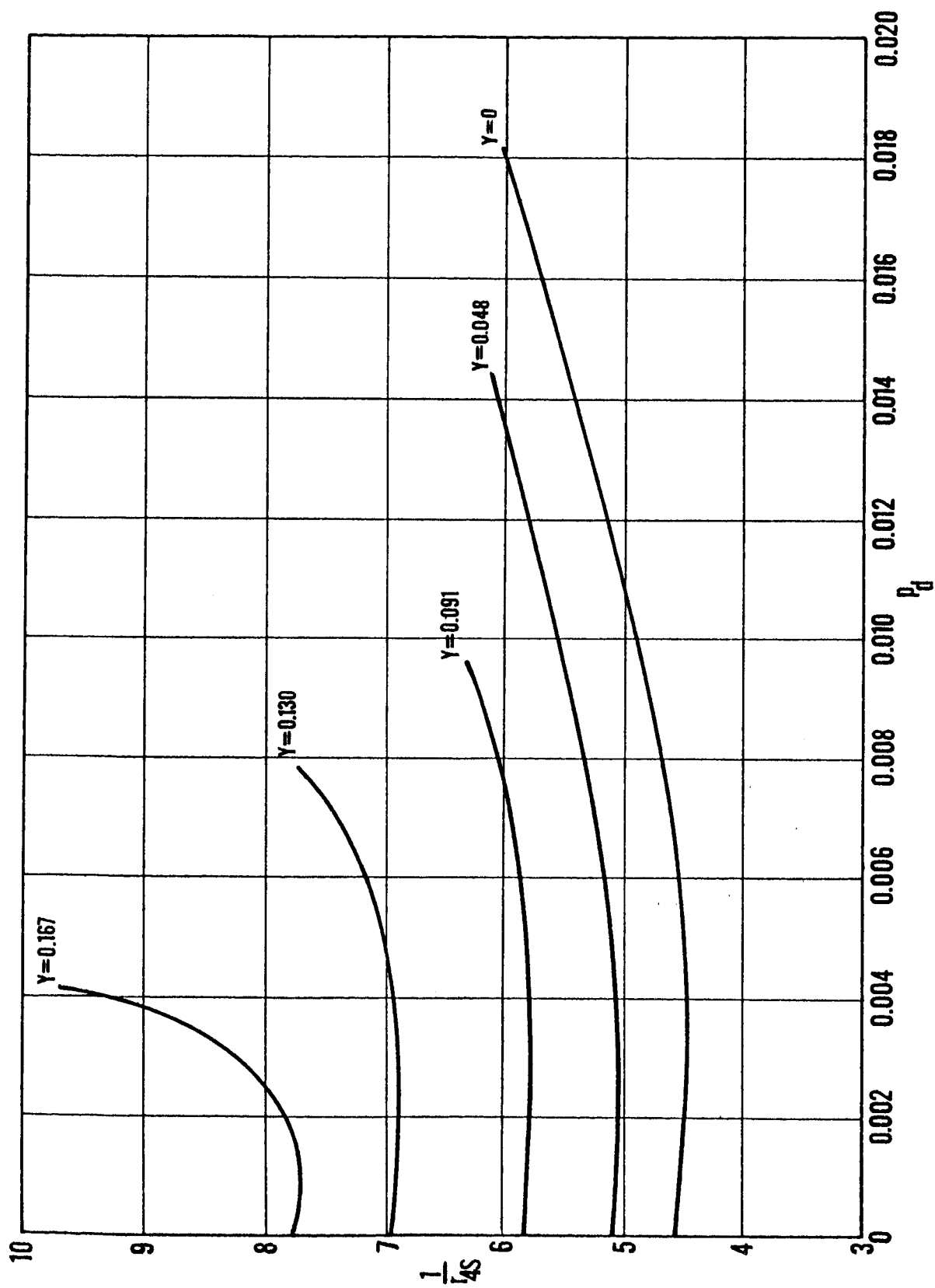


FIG.5.- OVERALL DENSITY RATIO VS NORMALIZED DYNAMIC PRESSURE AT STABILITY BOUNDARY
 ($l_i = 2.5, l_e = 0.2$)

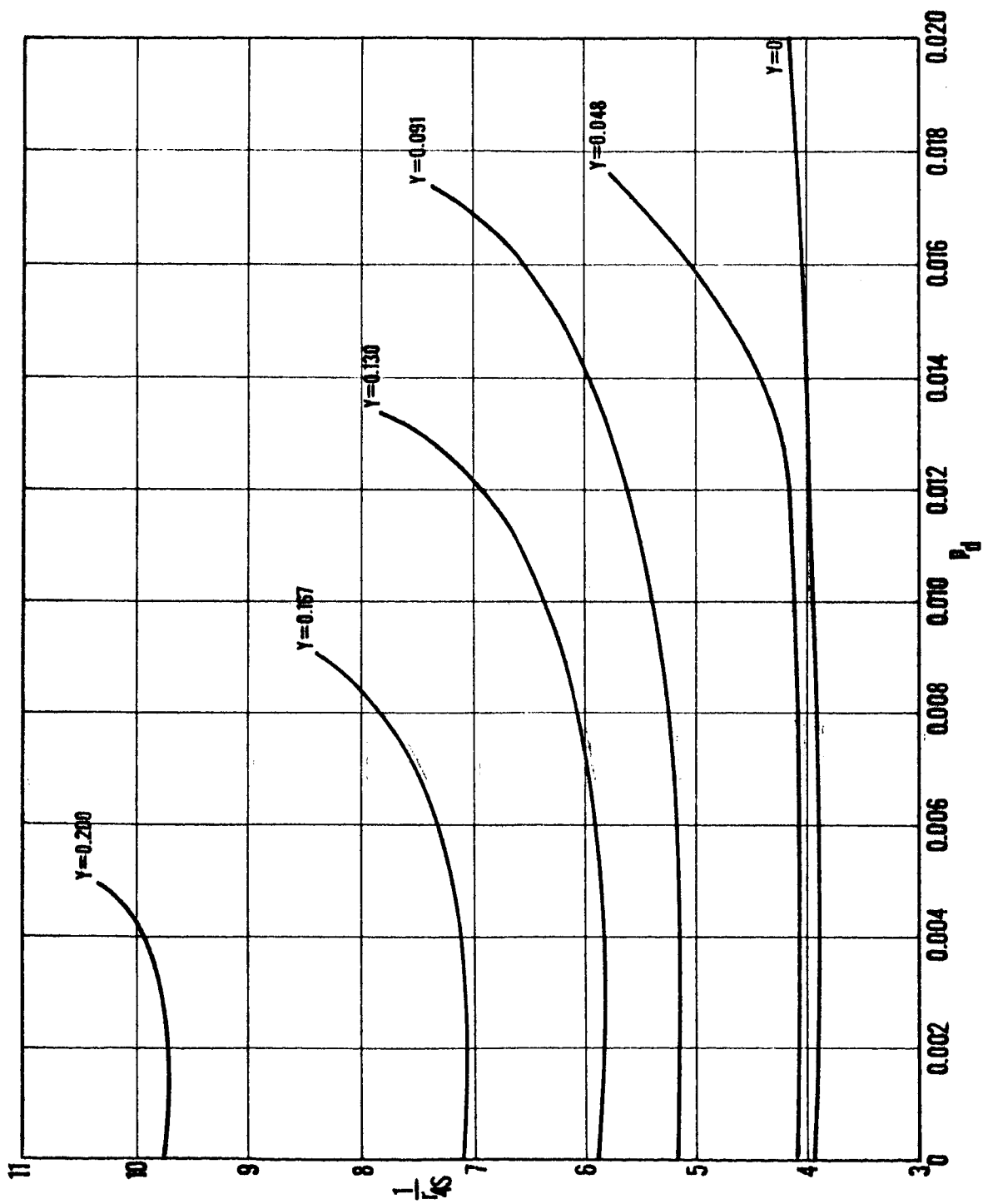


FIG. 6. - OVERALL DENSITY RATIO VS NORMALIZED DYNAMIC PRESSURE AT STABILITY BOUNDARY
 ($l_i = 2.5$, $l_e = 0.5$)

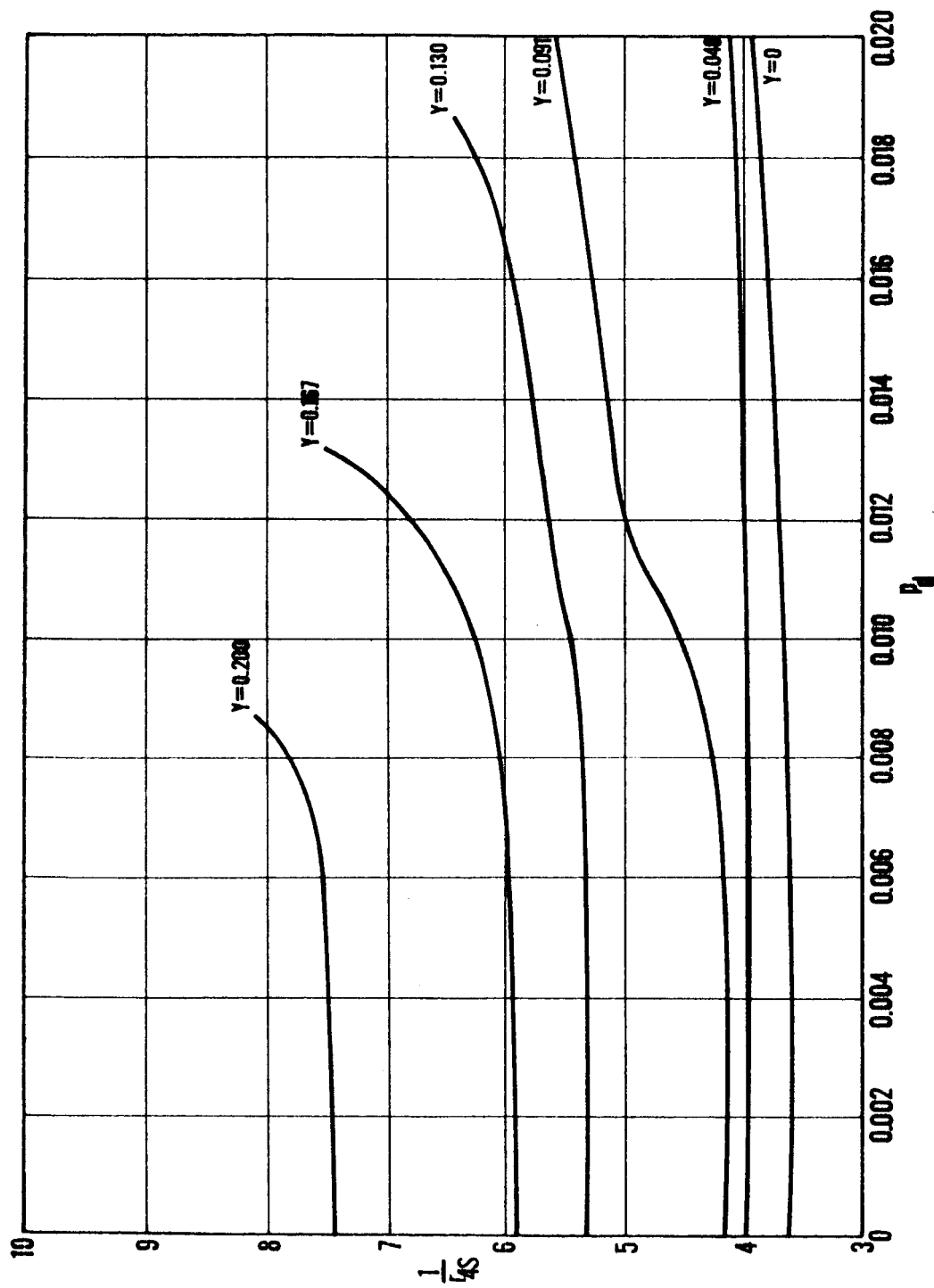


FIG. 7.- OVERALL DENSITY RATIO VS NORMALIZED DYNAMIC PRESSURE AT STABILITY BOUNDARY
 ($l_j = 2.5, l_e = 1.0$)

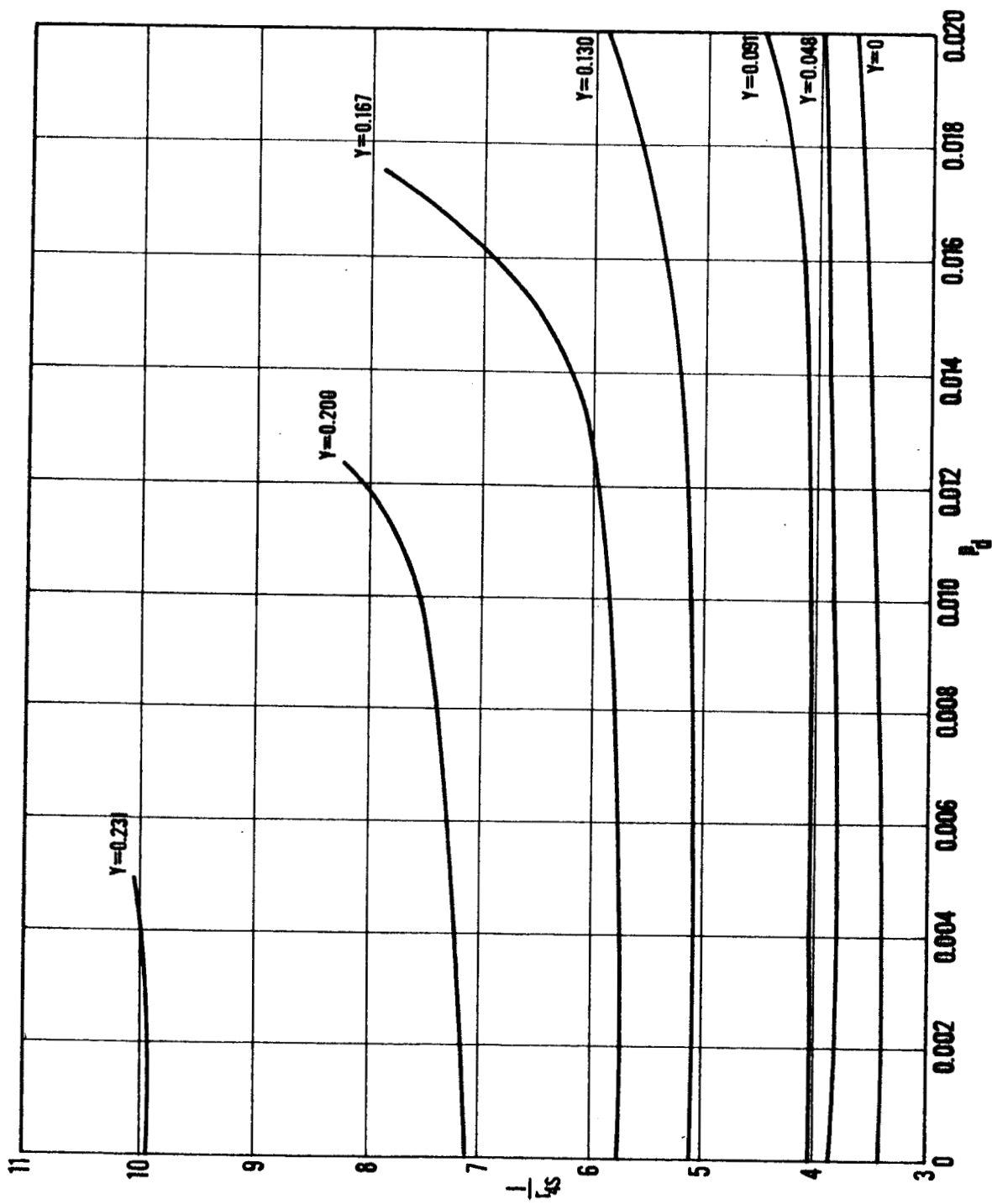


FIG.8. - OVERALL DENSITY RATIO VS NORMALIZED DYNAMIC PRESSURE AT STABILITY BOUNDARY
 ($I_j=2.5$, $I_e=1.5$)

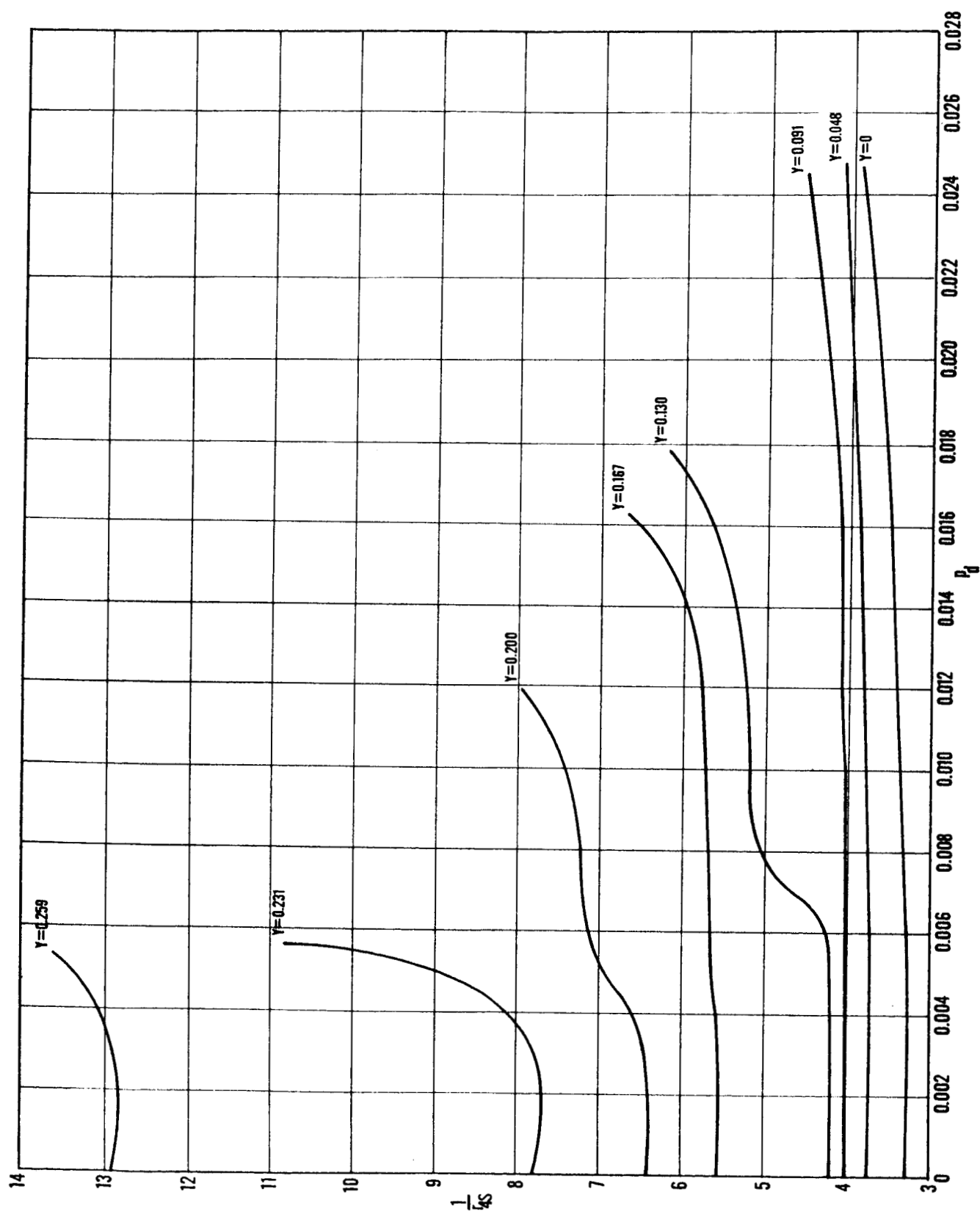


FIG. 9.—OVERALL DENSITY RATIO VS NORMALIZED DYNAMIC PRESSURE AT STABILITY BOUNDARY ($I_i=3.17$, $I_e=2.17$)

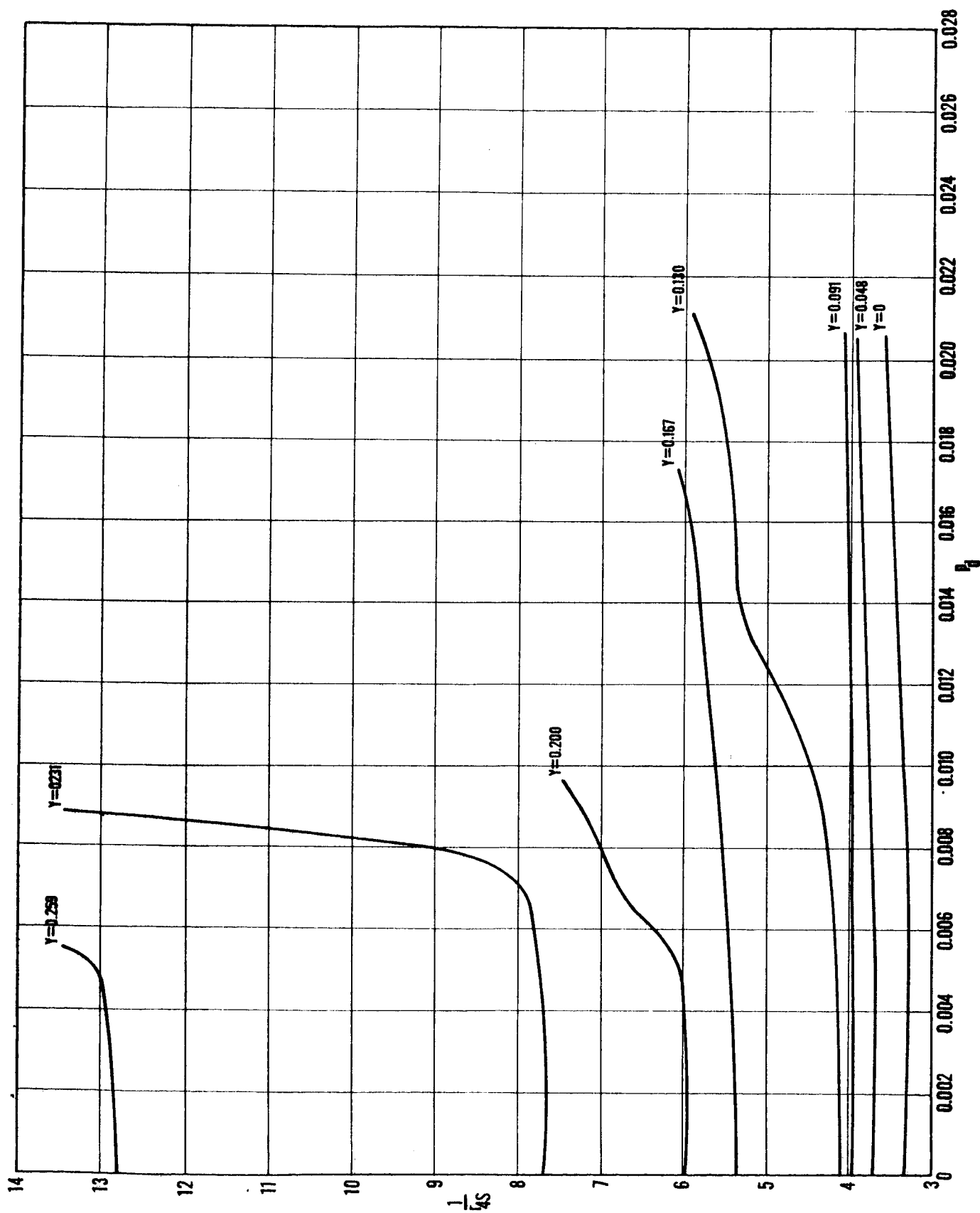


FIG. 10.— OVERALL DENSITY RATIO VS NORMALIZED DYNAMIC PRESSURE AT STABILITY BOUNDARY ($l_i = 3.67$, $l_e = 2.67$)

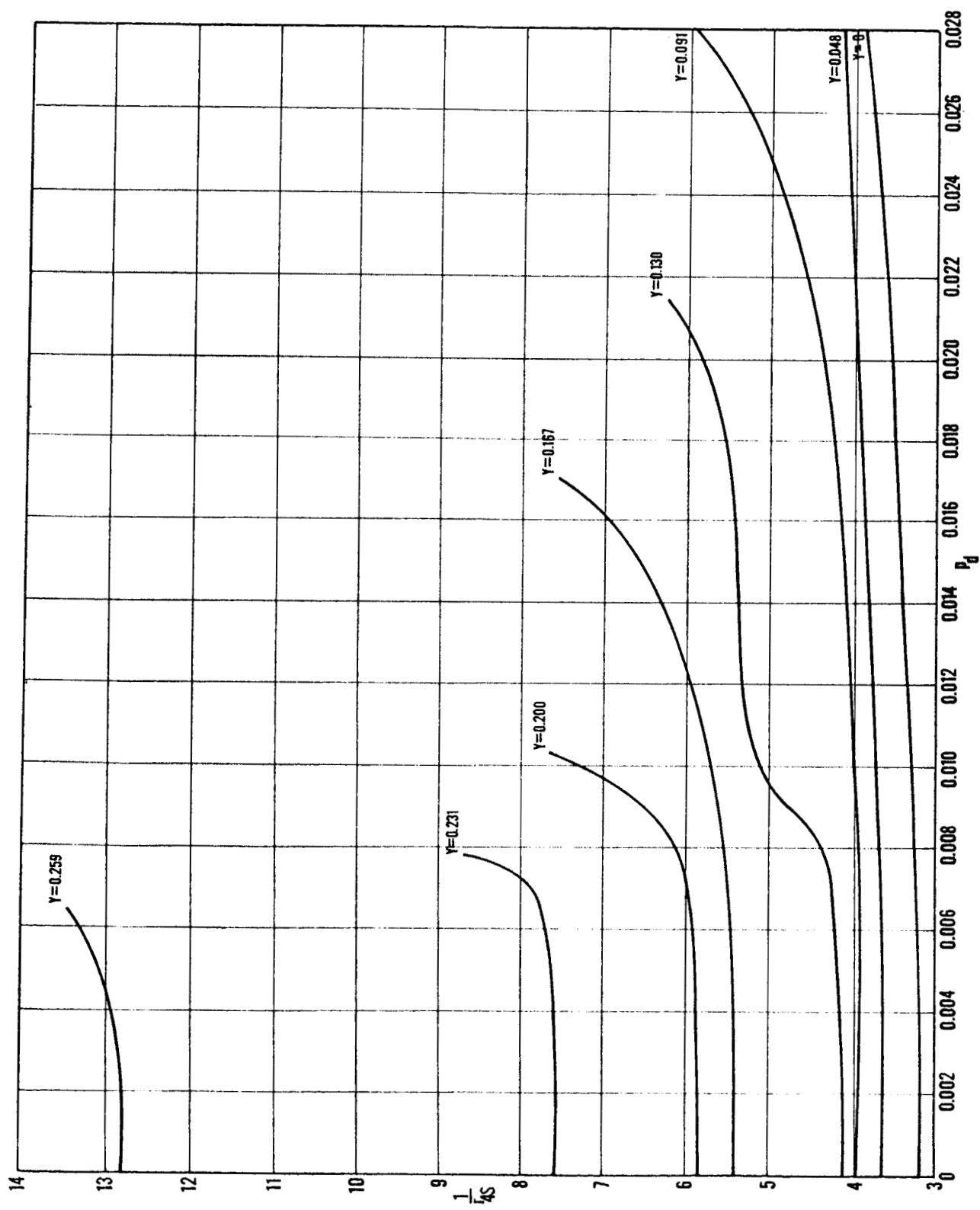


FIG.11.- OVERALL DENSITY RATIO VS NORMALIZED DYNAMIC PRESSURE AT STABILITY BOUNDARY ($I_i=4.5$, $I_e=3.5$)

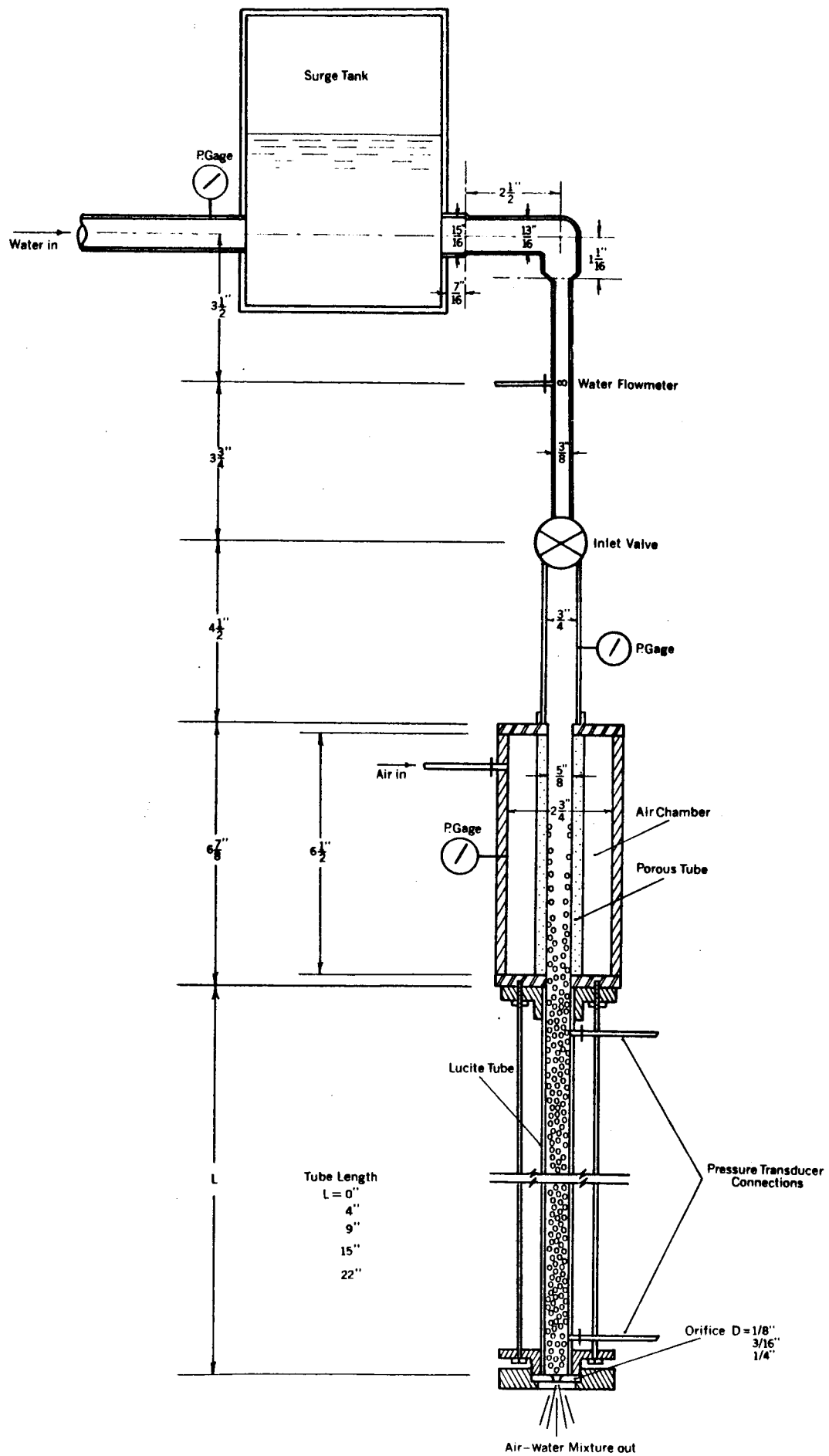


FIG. 12.- AIR-WATER APPARATUS TEST SECTION

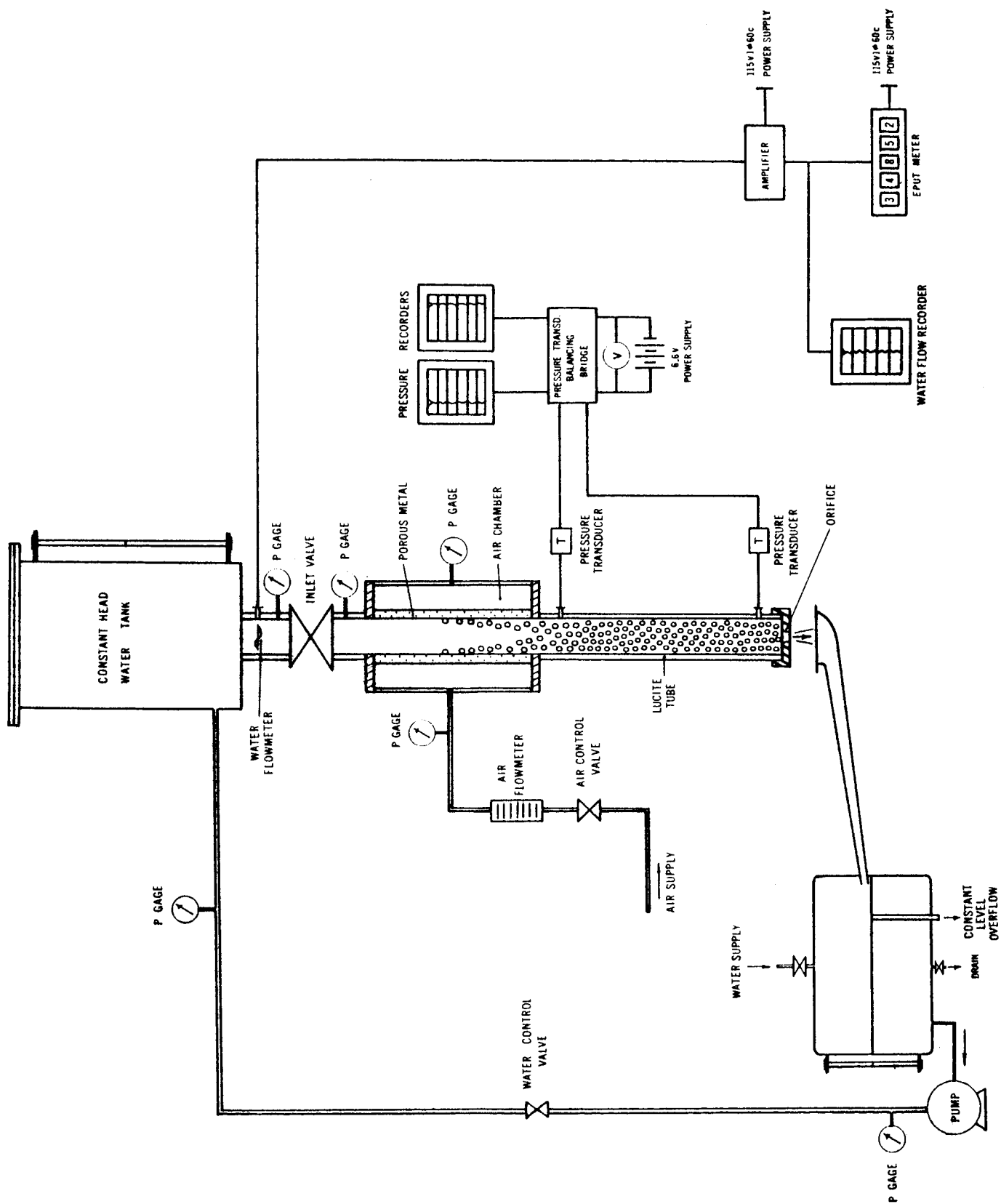


FIGURE 13.- SCHEMATIC DIAGRAM OF EXPERIMENTAL SET-UP FOR TWO-PHASE INSTABILITY [AIR-WATER APPARATUS]

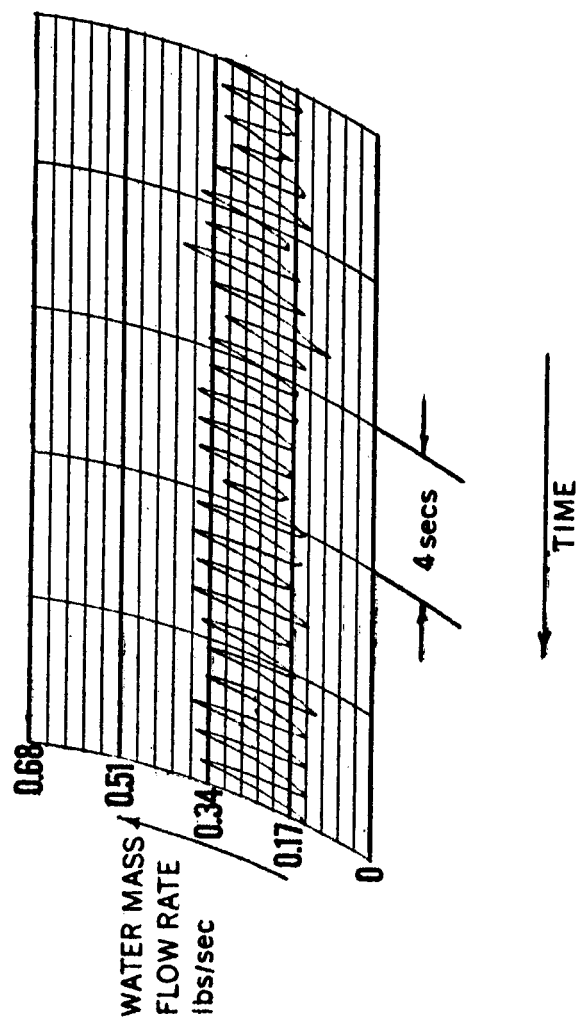


FIG.14.— A RECORDING OF WATER MASS FLOW RATE OSCILLATIONS NEAR STABILITY BOUNDARY

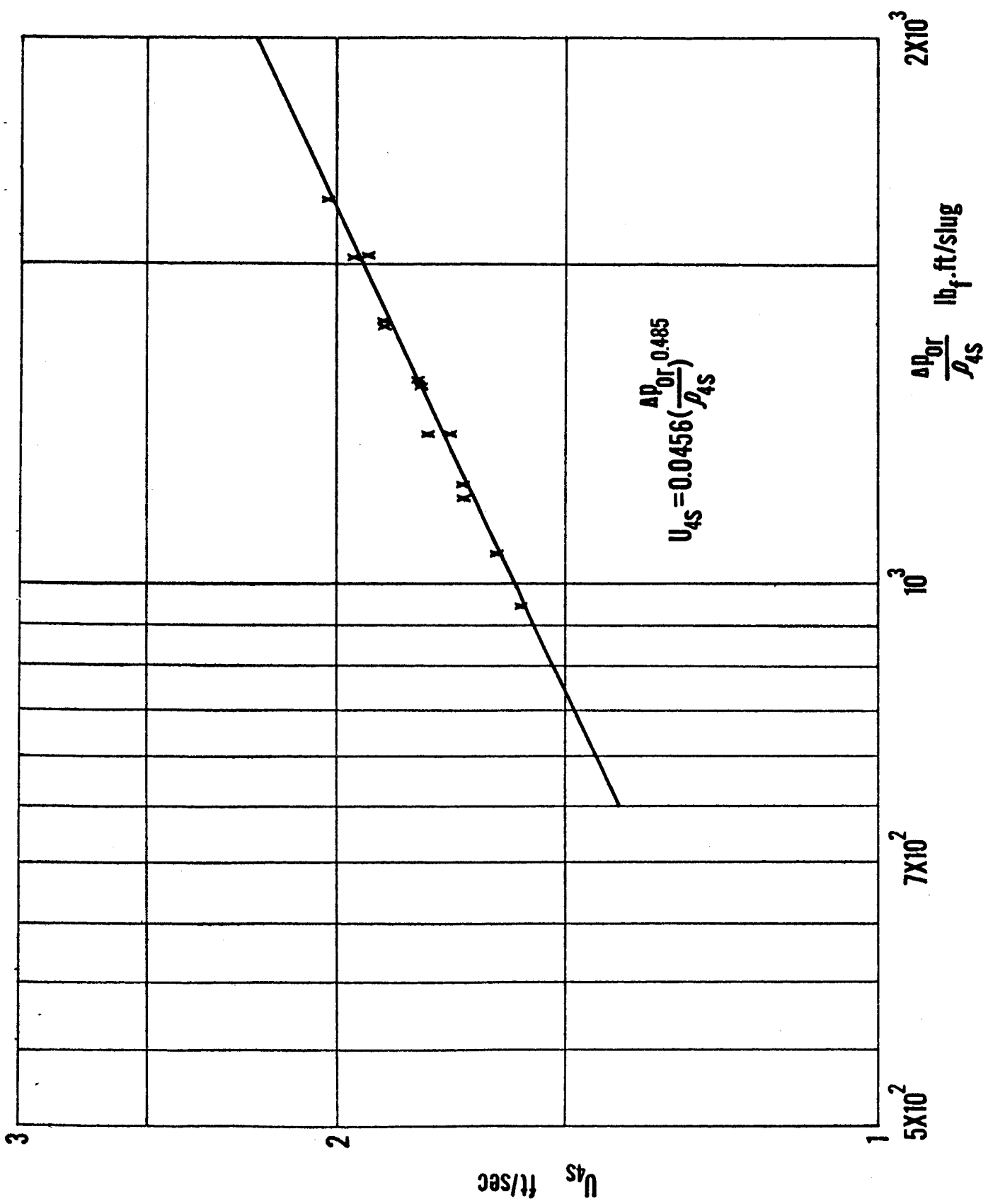


FIG.15. — 1/8" DIA. ORIFICE CALIBRATION FOR TWO-PHASE FLOW

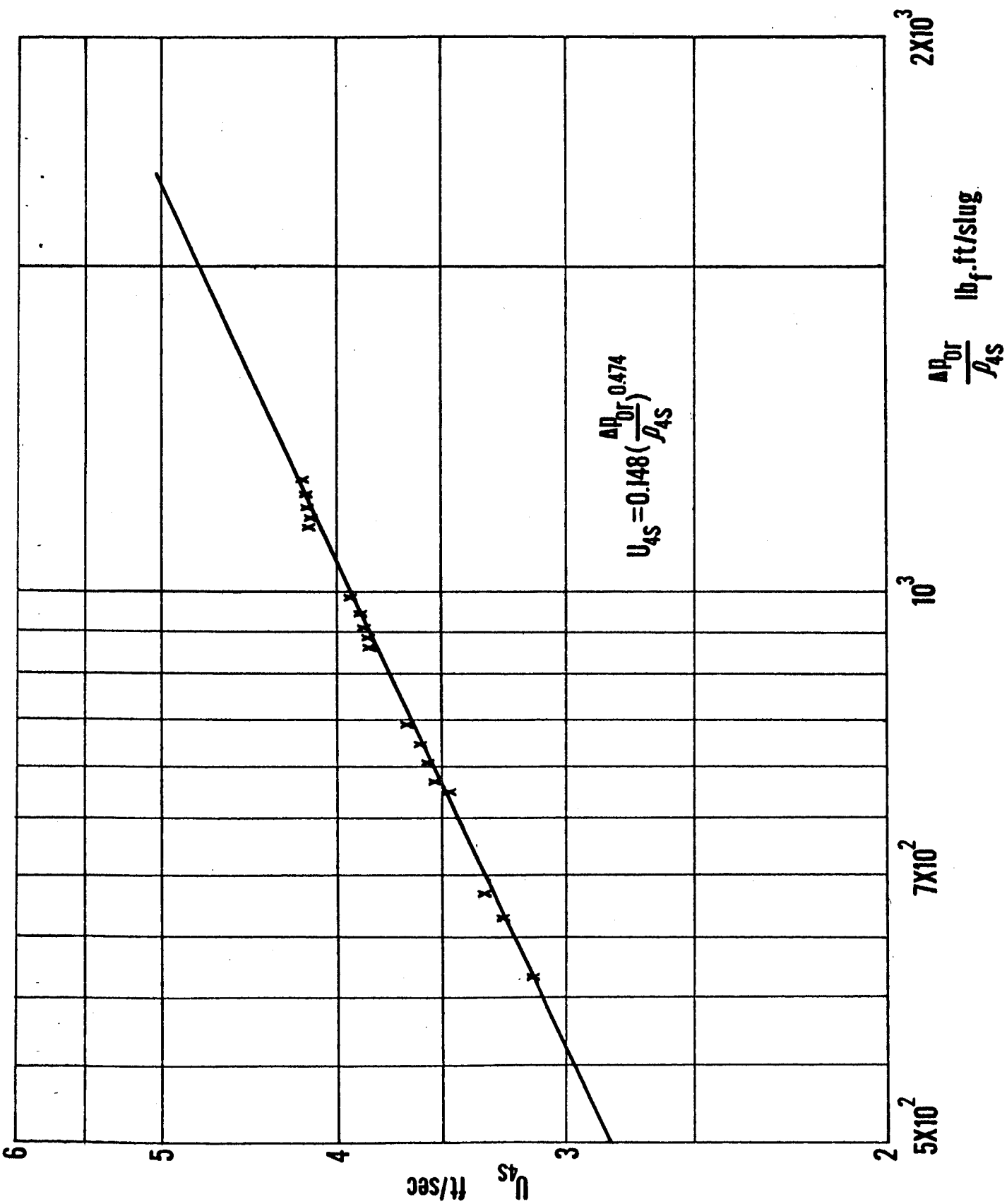


FIG.16. — 3/16" DIA. ORIFICE CALIBRATION FOR TWO-PHASE FLOW

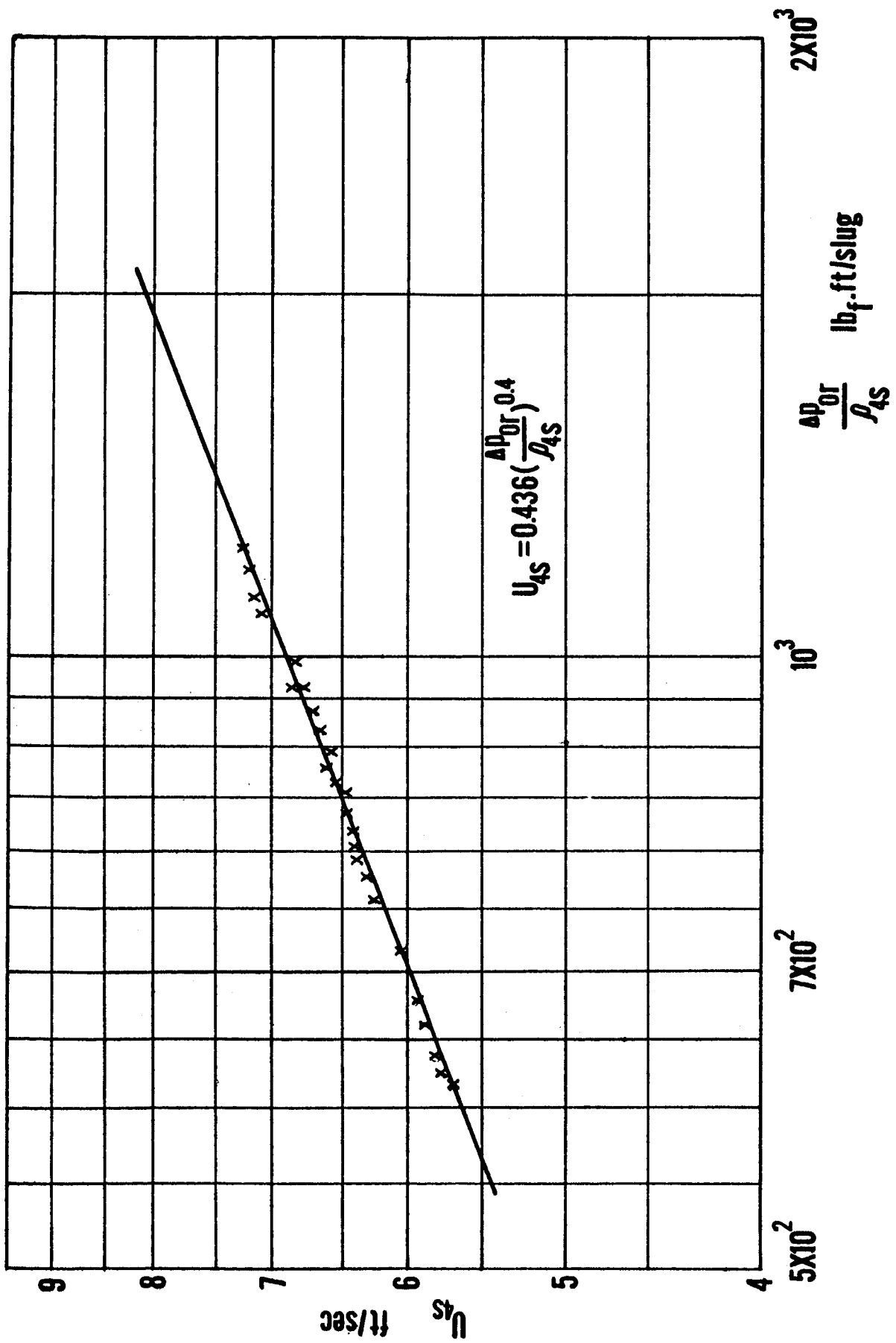


FIG.17.—1/4" DIA. ORIFICE CALIBRATION FOR TWO-PHASE FLOW

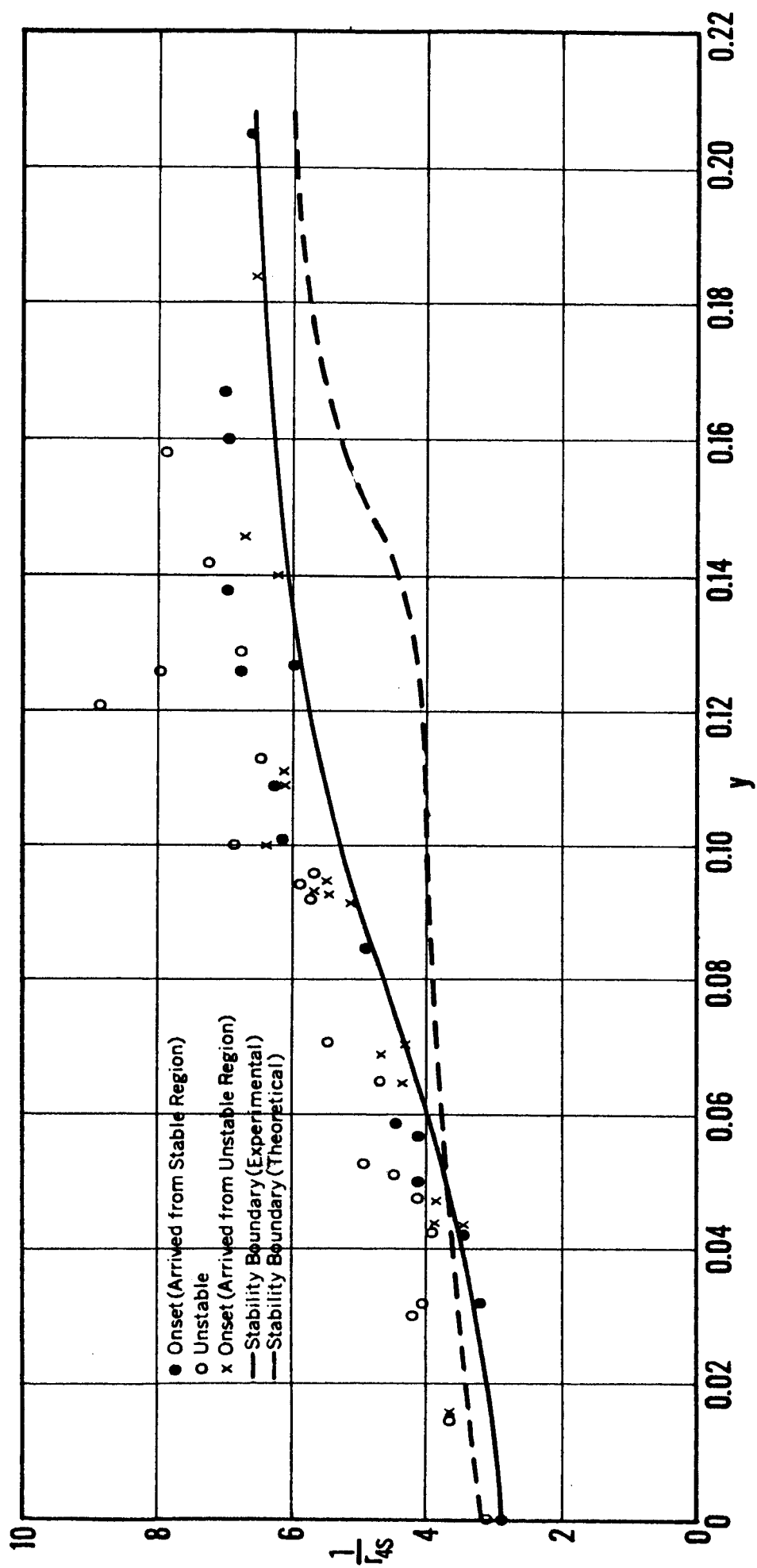


FIG.18.— EXPERIMENTAL AND THEORETICAL STABILITY BOUNDARY ($L_e = 22$ in., $D_{or} = 1/8$ in)

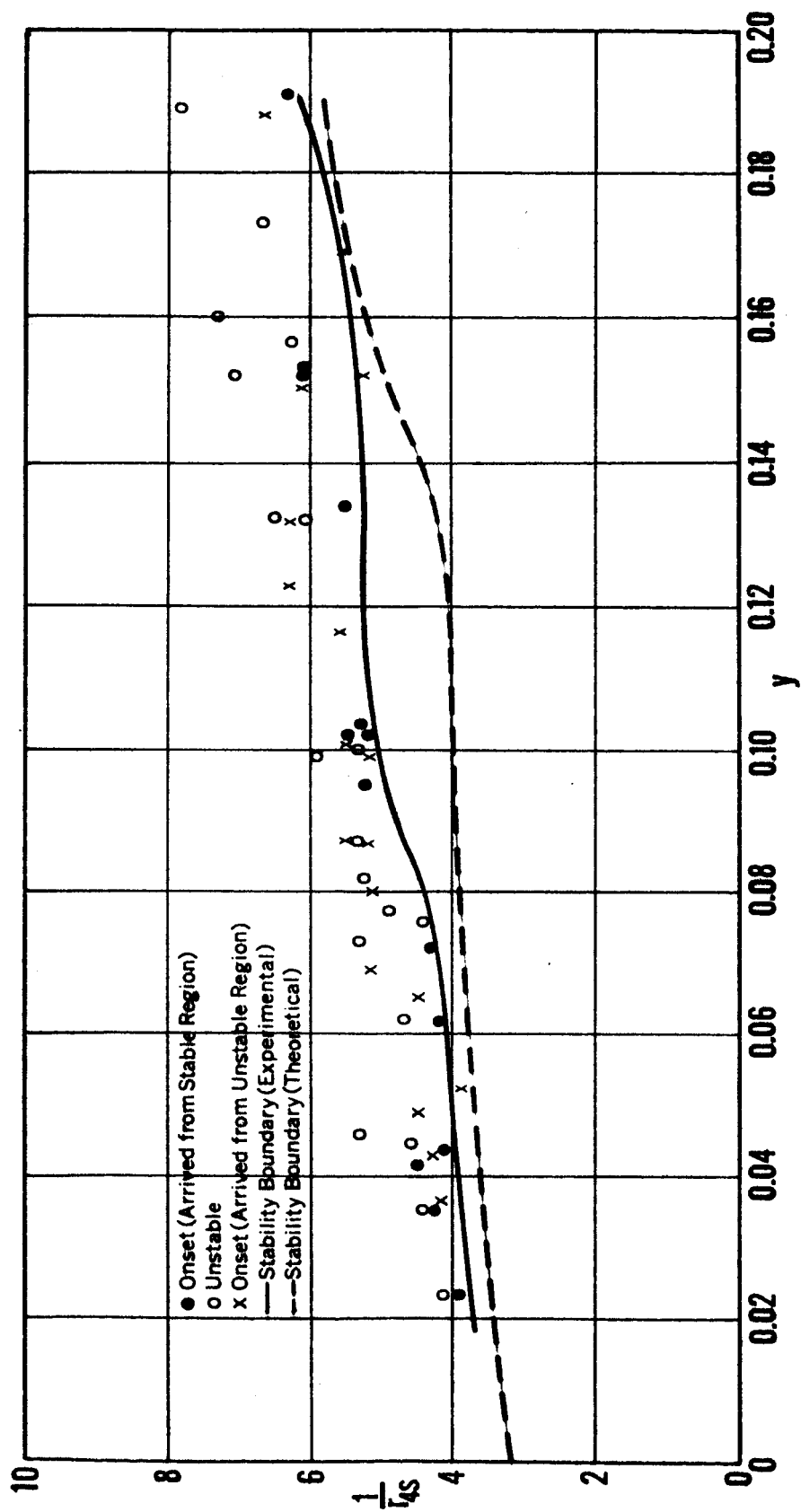


FIG.19.— EXPERIMENTAL AND THEORETICAL STABILITY BOUNDARY ($L_g = 22$ in., $D_{gr} = 3/16$ in.)

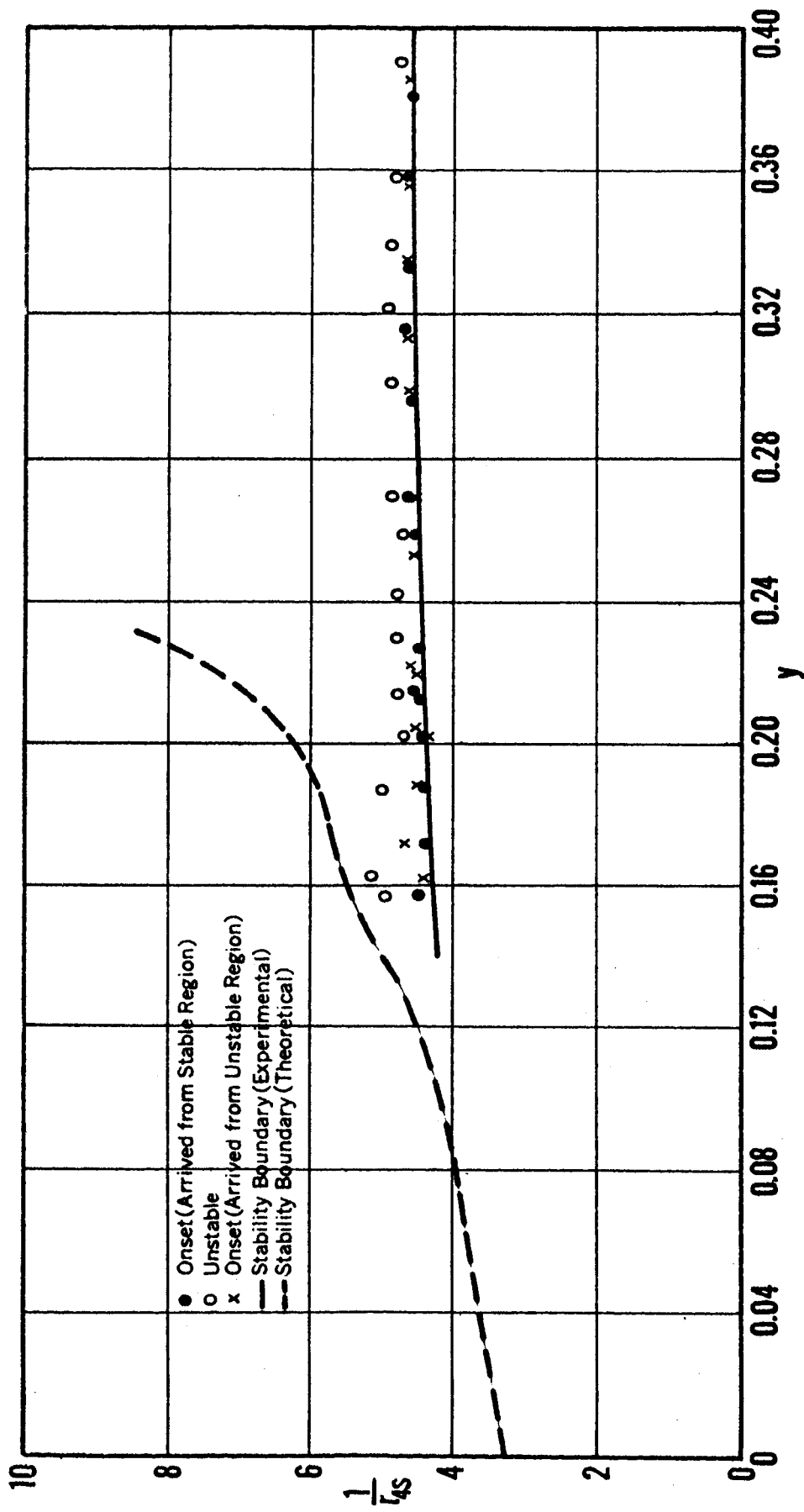


FIG. 20. — EXPERIMENTAL AND THEORETICAL STABILITY BOUNDARY ($L_e = 22$ in., $D_{or} = 1/4$ in.)

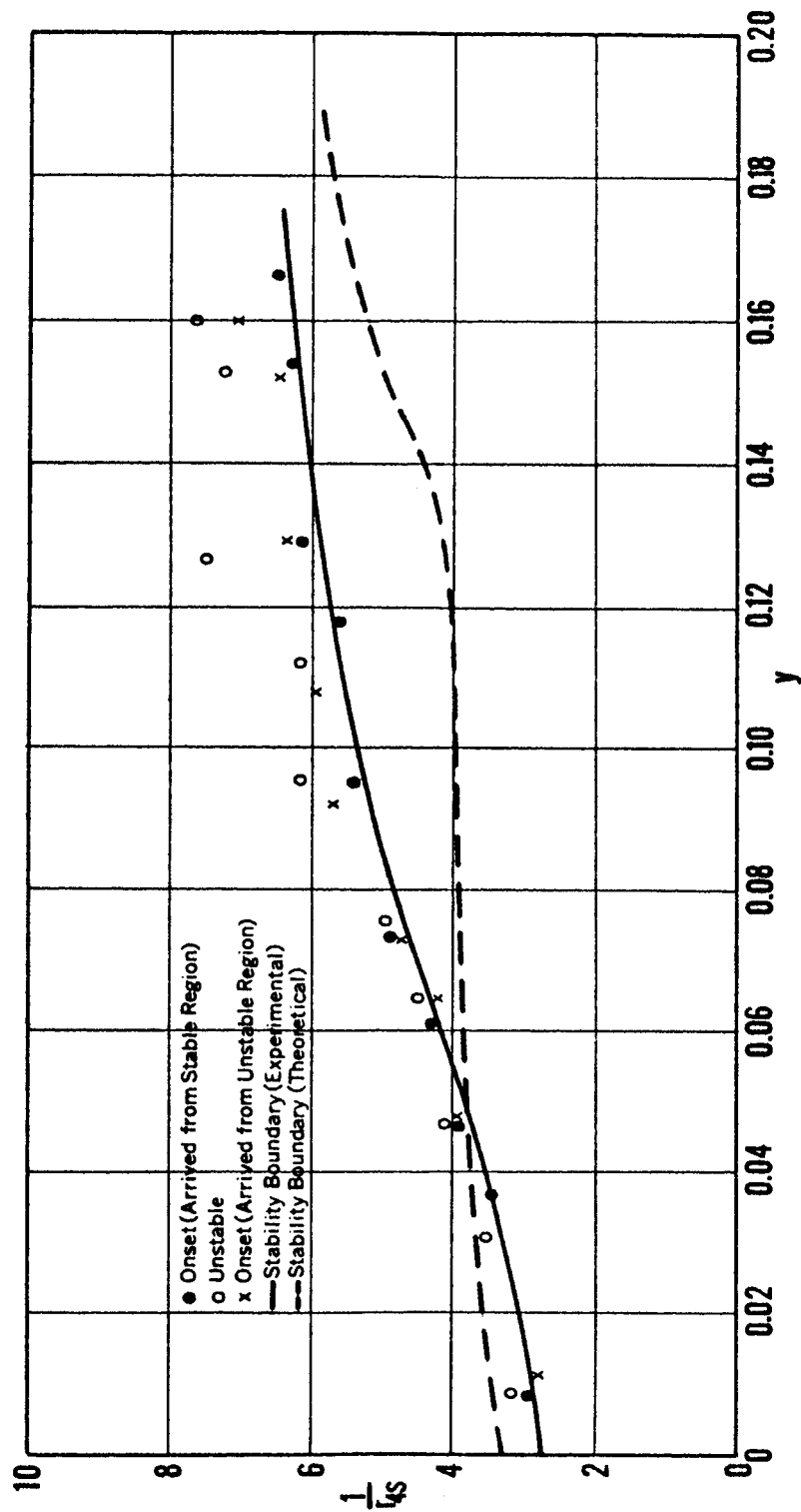


FIG. 21.— EXPERIMENTAL AND THEORETICAL STABILITY BOUNDARY ($L_e=15$ in., $D_{or}=1/8$ in.)

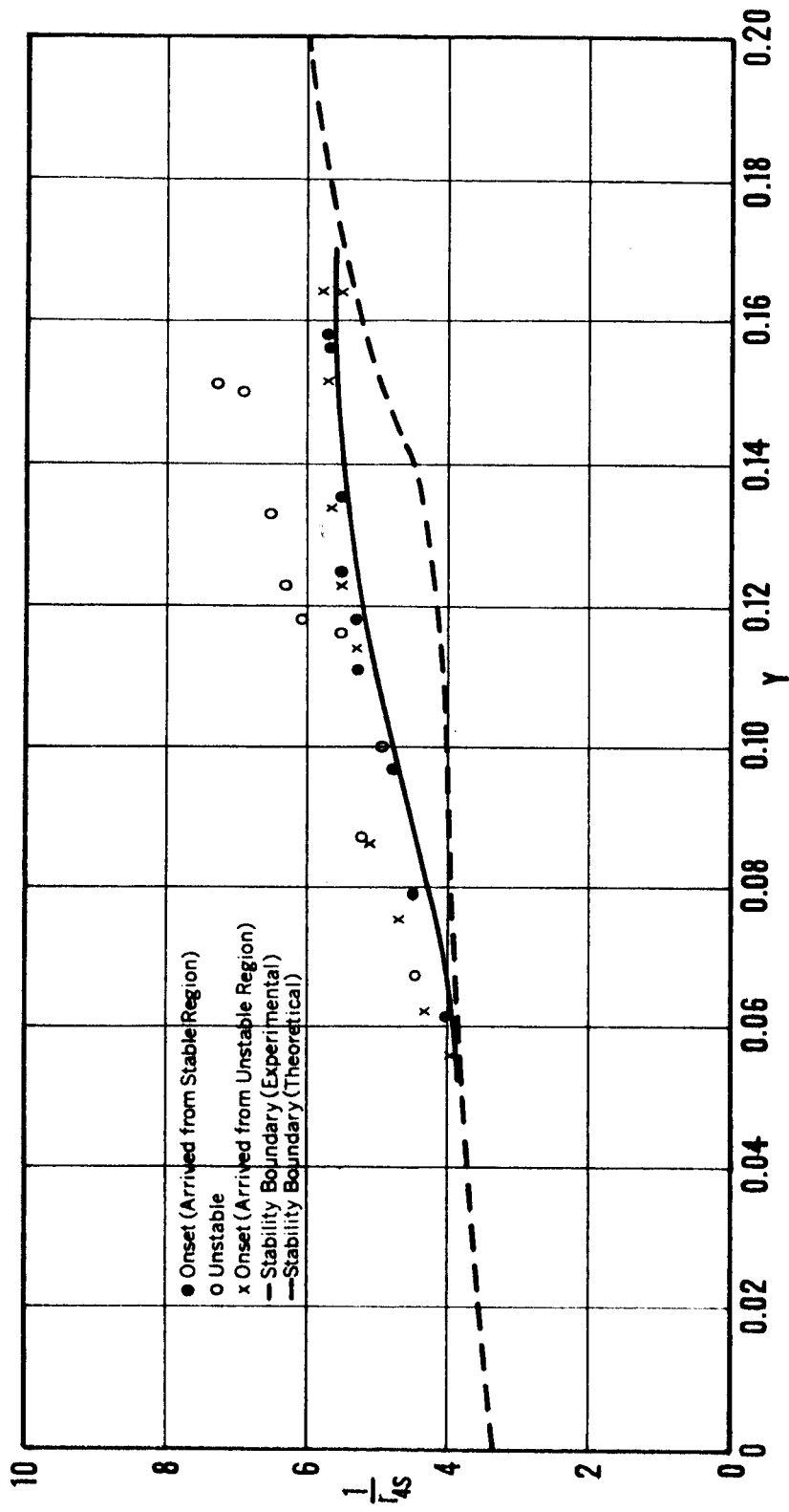


FIG. 22. — EXPERIMENTAL AND THEORETICAL STABILITY BOUNDARY ($L_e = 15 \text{ in.}$, $D_{or} = 3/16 \text{ in.}$)

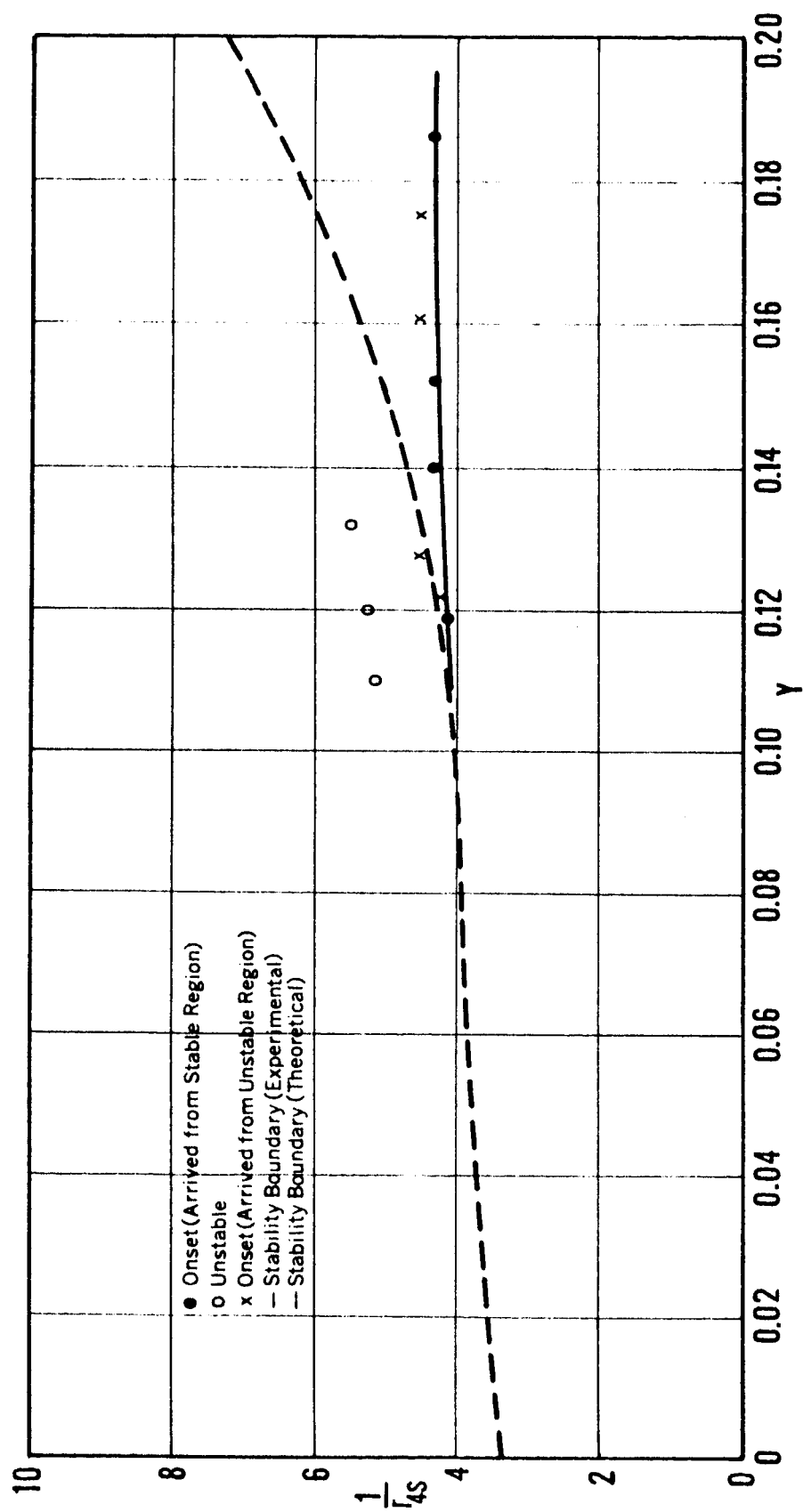


FIG.23. — EXPERIMENTAL AND THEORETICAL STABILITY BOUNDARY ($L_e = 15 \text{ in.}$, $D_{or} = 1/4 \text{ in.}$)

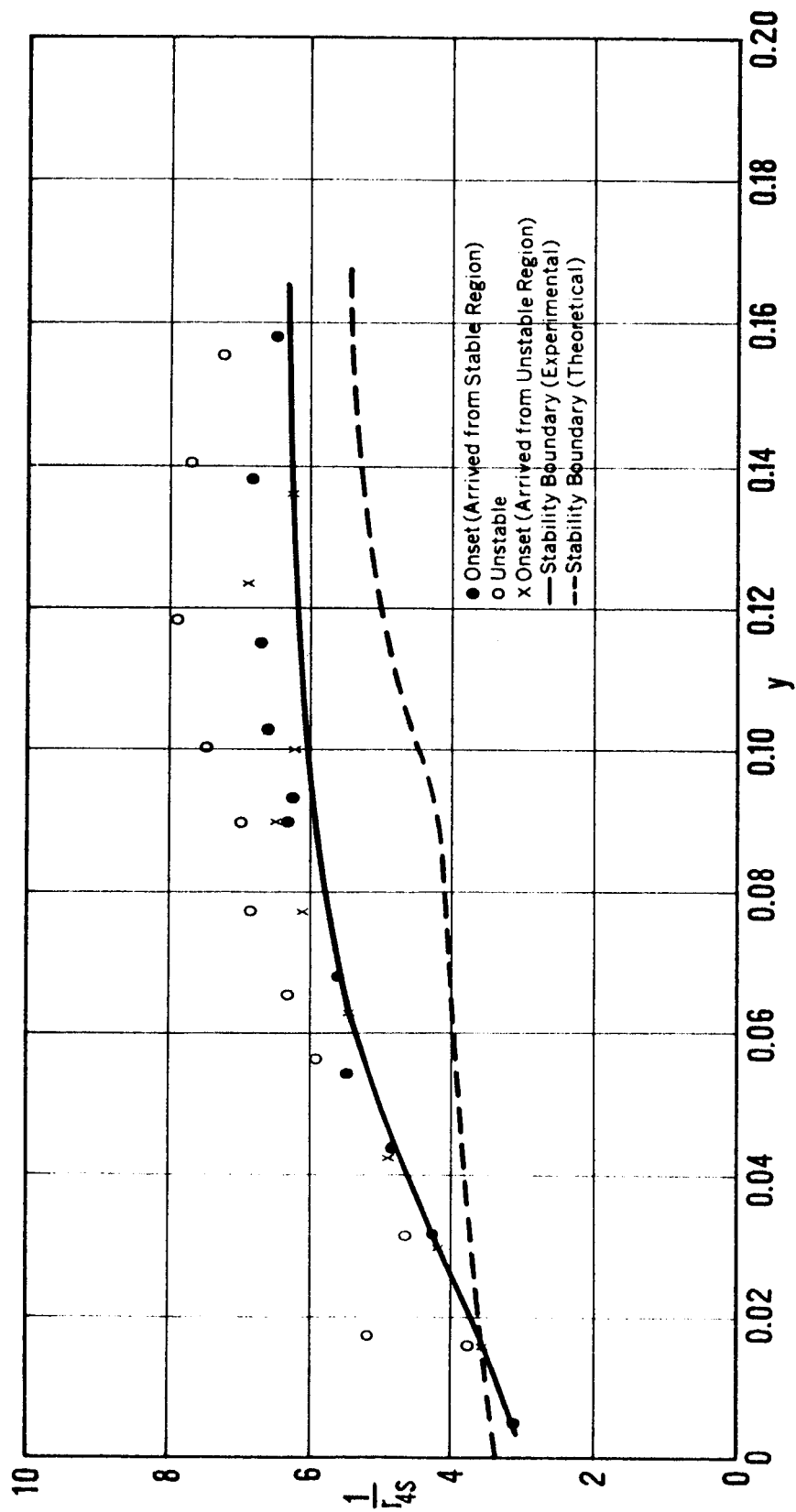


FIG. 24.— EXPERIMENTAL AND THEORETICAL STABILITY BOUNDARY ($L_e = 9 \text{ in.}$, $D_{0r} = 1/8 \text{ in.}$)

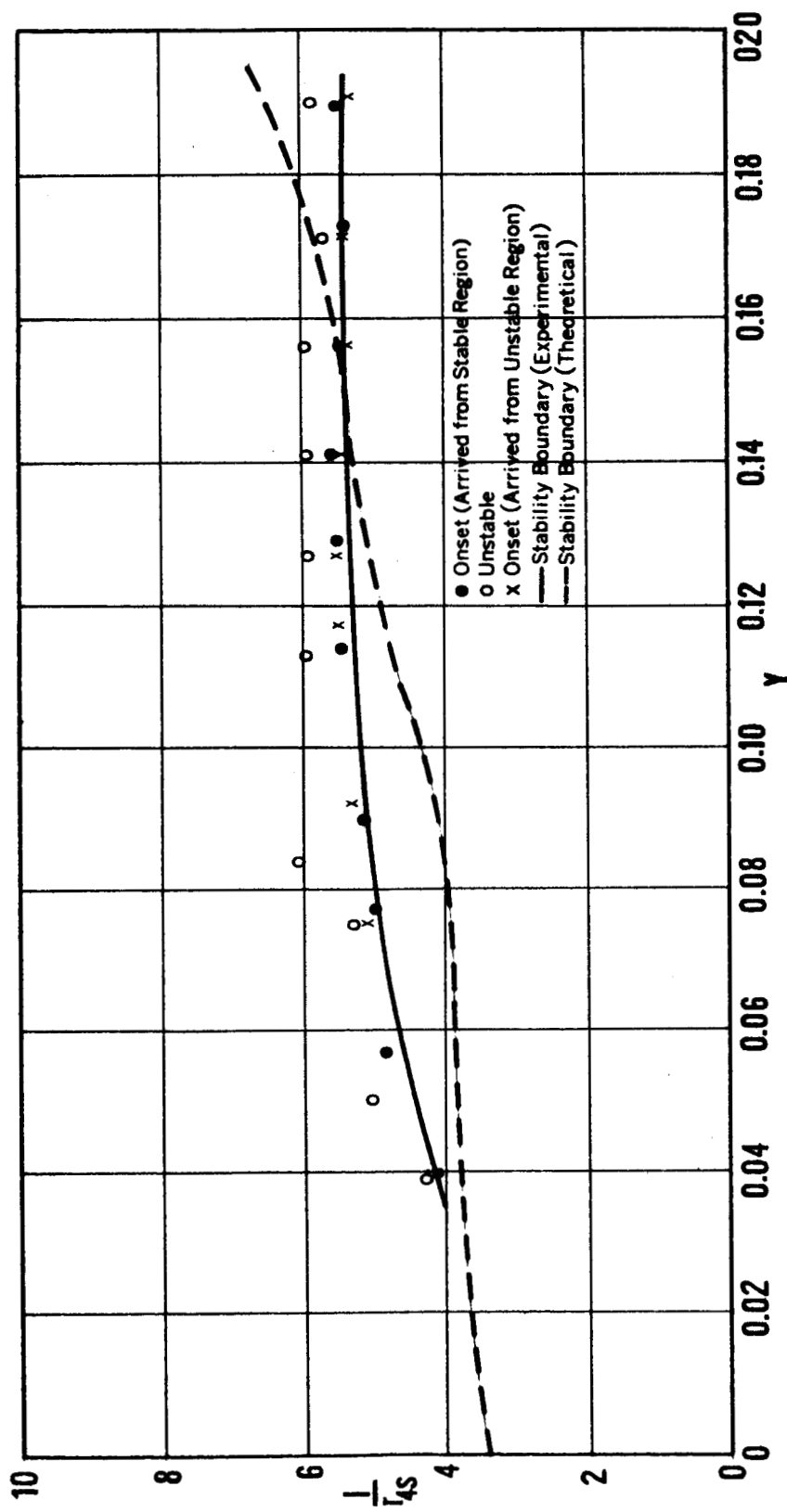


FIG.25.— EXPERIMENTAL AND THEORETICAL STABILITY BOUNDARY ($L_e = 9$ in., $D_{or} = 3/16$ in.)

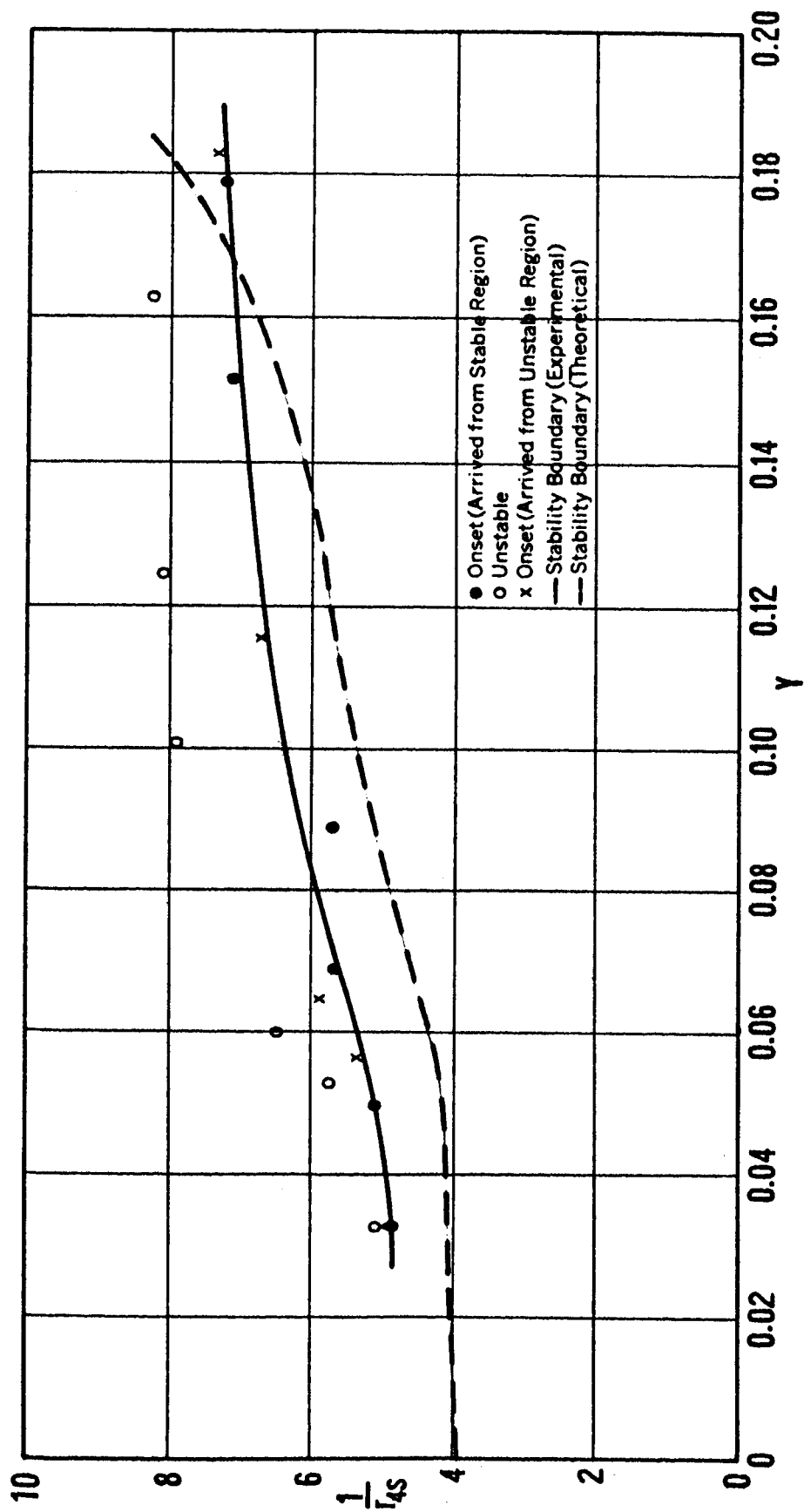


FIG. 26. — EXPERIMENTAL AND THEORETICAL STABILITY BOUNDARY ($L_e = 4$ in., $D_{or} = 1/8$ in.)

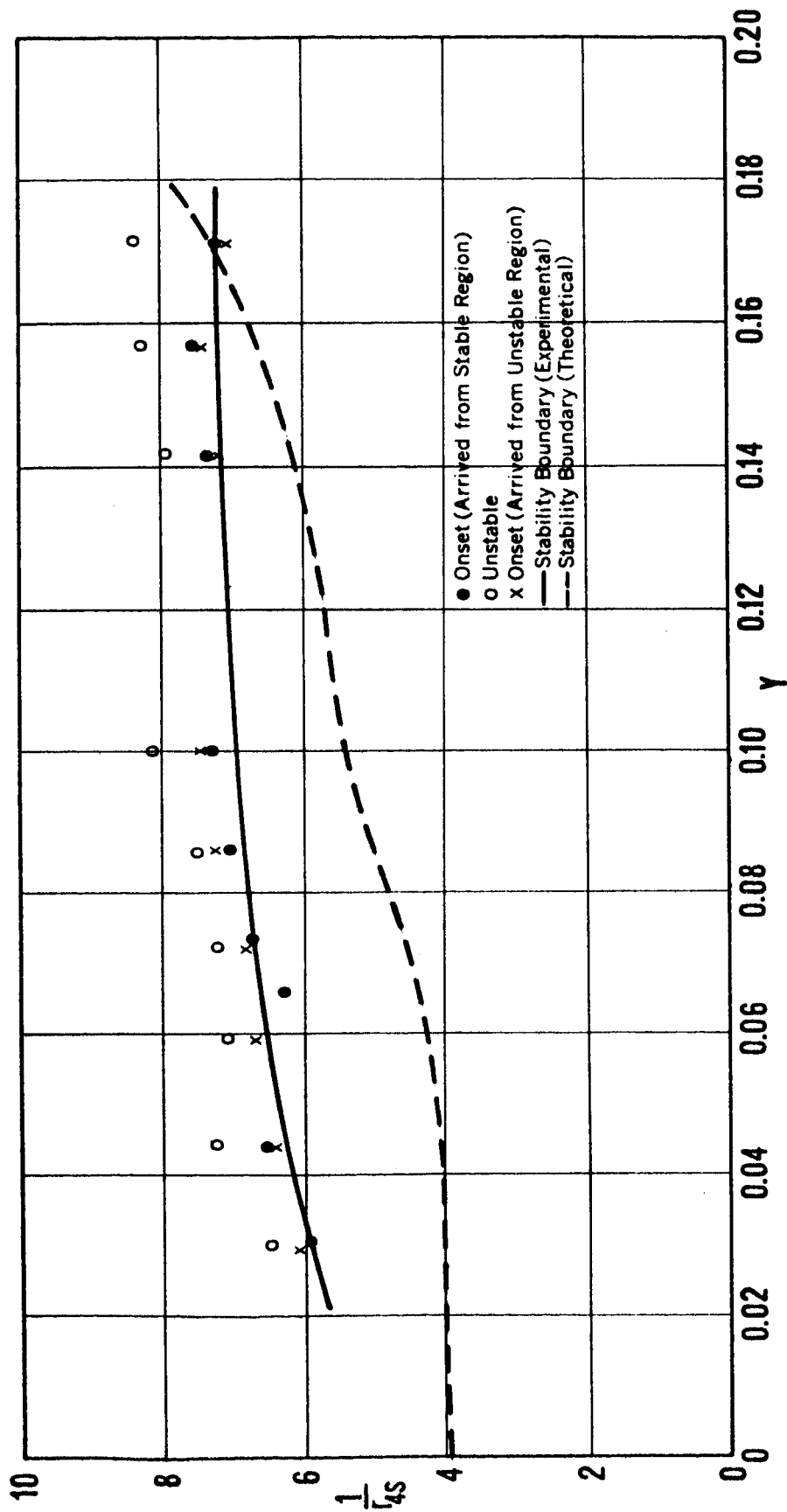


FIG.27. — EXPERIMENTAL AND THEORETICAL STABILITY BOUNDARY ($L_e = 4$ in., $D_{or} = 3/16$ in.)

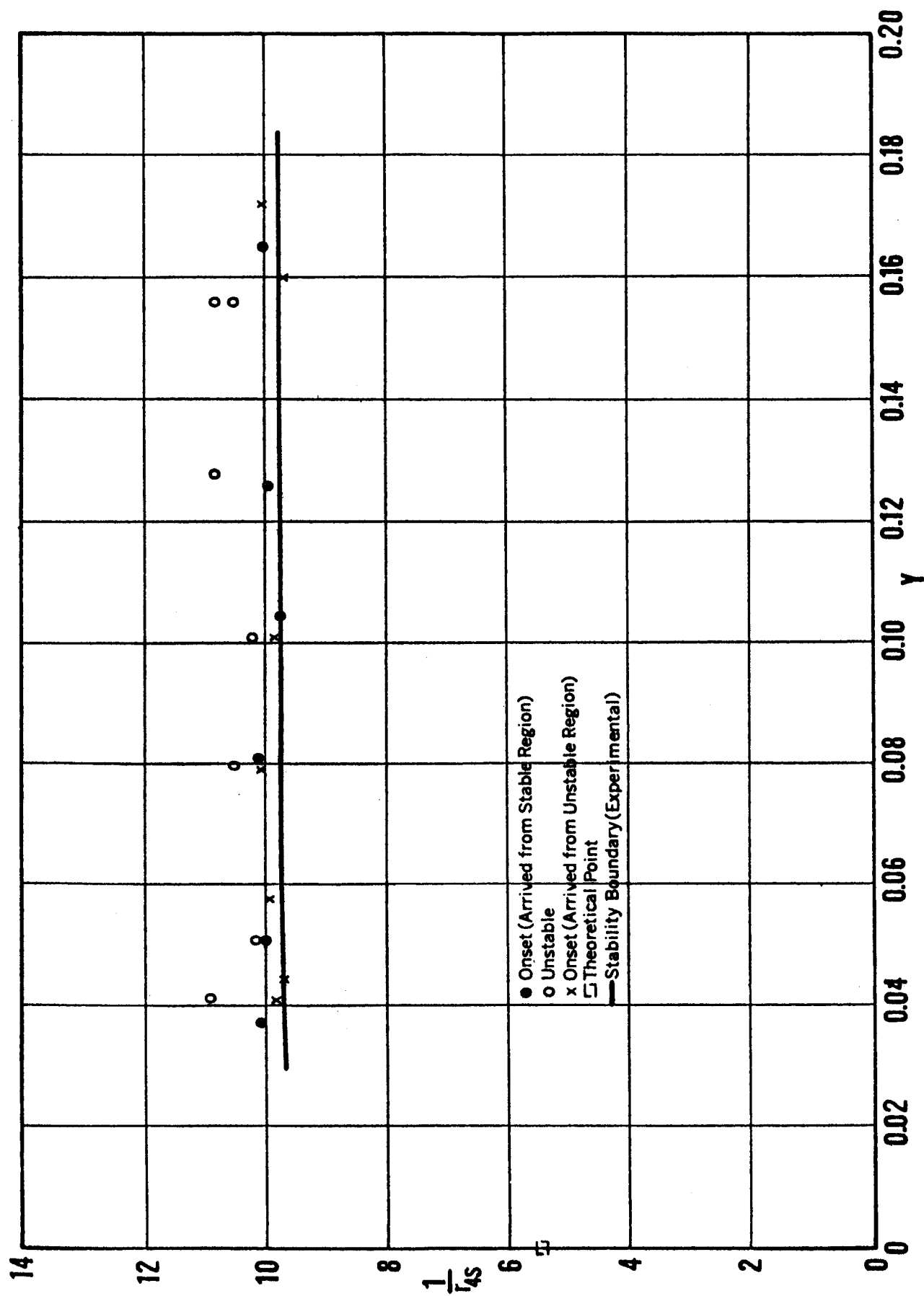


FIG.28.— EXPERIMENTAL AND THEORETICAL STABILITY BOUNDARY ($L_e=0$, $D_{or}=1/8$ in.)

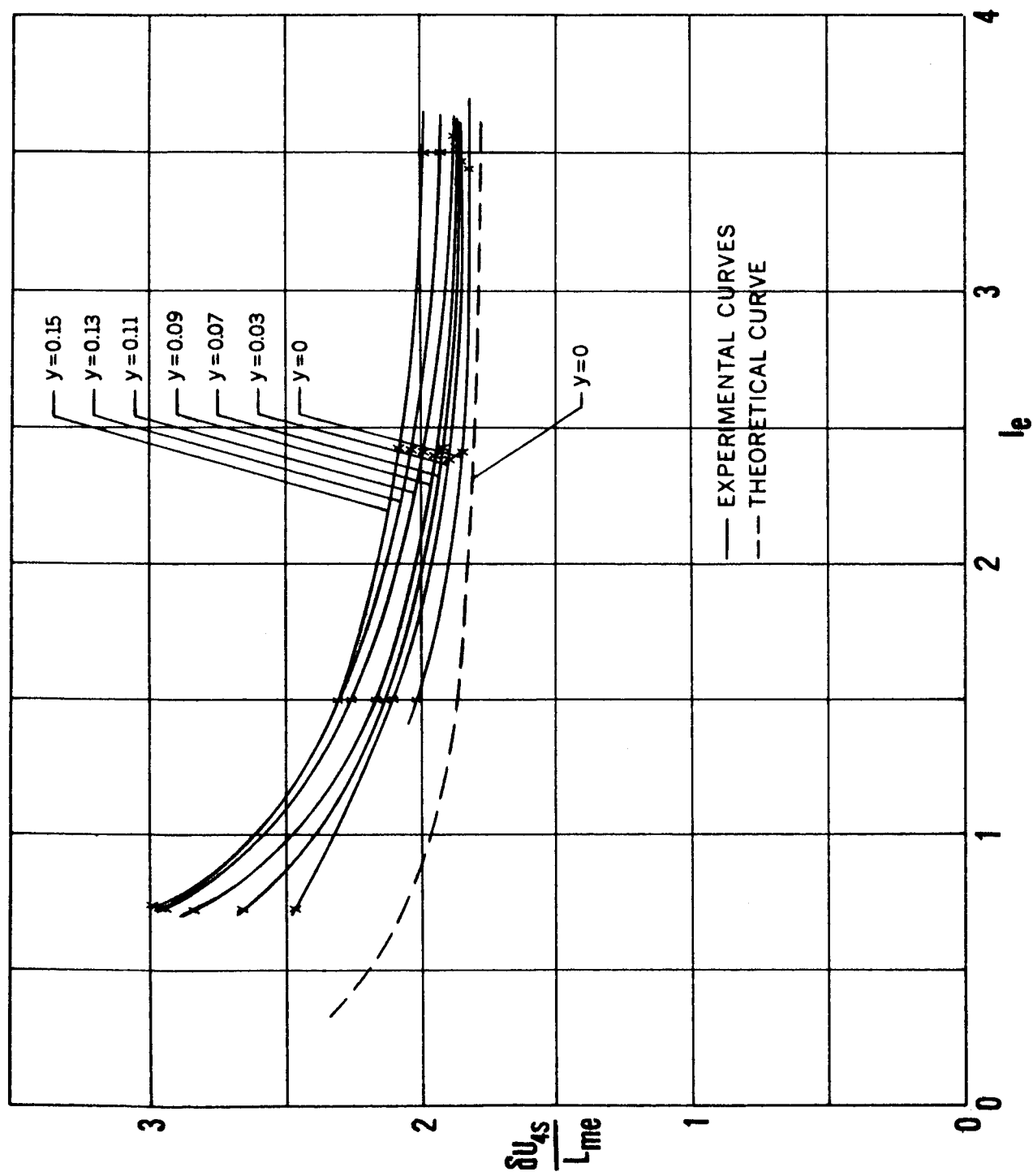


FIG.29. - TIME PERIOD OF OSCILLATIONS AT STABILITY BOUNDARY